# RESEARCH ACTIVITIES

## Materials Molecular Science

Extensive developments of new molecules, molecular systems, and their higher-order assemblies are being conducted in three Divisions of Electronic Structures, Electronic Properties, and Molecular Functions, one division for visiting professors, and Research Center for Molecular Scale Nanoscience, in an attempt to discover new phenomena and useful functions. The physical properties of electronic, optical and magnetic properties on new functional materials are investigated, and moreover, the chemical properties like catalysis and photochemistry and technological applications like solar cells are also examined in this department.

# Novel Properties of Magnetic Ultrathin Films Studied by *In Situ* Spectroscopic Methods

**Department of Materials Molecular Science**
**Division of Electronic Structure**

| | |
|---|---|
| YOKOYAMA, Toshihiko | Professor |
| NAKAGAWA, Takeshi | Assistant Professor |
| TAKAGI, Yasumasa | Assistant Professor |
| EGUCHI, Keitaro | Graduate Student |
| NAKANO, Hirohito | Graduate Student* |
| FUNAKI, Yumiko | Secretary |
| TOYAMA, Yu | Secretary (Nanotechnology Platform project) |
| YASUI, Yuco | Secretary (Graduate school affairs) |

Novel properties of magnetic metal ultrathin films have been attractive both from fundamental interest and from technological requirements. We are especially interested in drastic modification of metal thin films through the film–substrate interaction and/or a surface chemical treatment. The magnetic properties are characterized by means of several kinds of *in situ* spectroscopic methods like MOKE (Magneto-Optical Kerr Effect) using UV-visible lasers and XMCD (X-ray Magnetic Circular Dichroism) using synchrotron radiation soft X-rays, and UV magnetic circular dichroism photoelectron emission microscopy (UV MCD PEEM) using such ultrashort pulsed UV lasers.

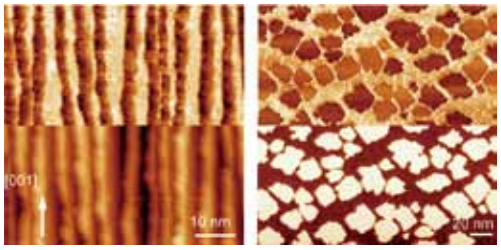


**Figure 1.** STM images of nanowires for Fe 0.3 ML (~6 atom width) (left) and nanodots for Fe 0.4 ML. The top and bottom panels correspond to the spin-polarized *dI*/*dV* and topographic images, respectively. The right-top panel clearly shows magnetically single domain dots (arrows denote the magnetization directions along [1-10]).

## 1. Giant Magnetic Anisotropy and Coercivity in Fe Island and Atomic Wire on W(110)[1)]

Hard magnets is an important industrial material both for data storage and power applications like electromotive actuators and power generators. Although the magnetic energy product ($BH_{max}$) that characterizes hard magnets has improved in the last century, rare earth (RE) magnets like $Nd_2Fe_{14}B$ have marked a saturation of the maximum available value of $BH_{max}$ = 500 kJ/m$^3$ since 1990. Moreover, the replacement of the RE has been demanded due to the scarcity of RE, and novel approaches to improve hard magnets have attracted interests. Magnetic nanostructures with single atomic layers have a possibility to manifest prominent magnetic properties such as magnetocrystalline anisotropy energy (MAE) and coercivity ($H_c$) that remarkably differ from the properties of bulk materials. The Fe monolayer on W(110) has been extensively studied as an ideal two-dimensional ferromagnetic system with a pseudomorphic growth mode and an extremely large strain due to a large difference in the lattice constants between Fe and W. Owing to its extreme hard magnet character, the anisotropy energy or the coercivity has not been directly determined from the hard axis magnetization curve measurements. In this work, we directly measure the giant MAE as well as large coercivity in Fe nanodots and nanowires grown on W(110) by using our ultrahigh vacuum superconducting magnet XMCD system installed in UVSOR-II. A remarkable difference between the dots and the stripes is found in the coercivity, although the MAE is similar for both systems.

Figure 1 shows the spin-polarized and topographic STM (scanning tunnel microscopy) images of Fe nanowires and nanodots. The measurements were performed in Johannes Gutenberg Mainz University through the collaboration with Prof. H. J. Elmers group. In the spin-polarized STM image of the nanodots, a clear contrast (darker and brighter islands) can be seen, implying that the nanodots are magnetically ordered as single domains with the magnetization easy axis of the [1-10] crystal axis.

Figure 2 shows the anisotropic magnetization curves of Fe 0.25 ML nanodots and nanowires at 5 K taken by measuring the Fe $L_3$-edge circularly polarized X-ray absorption intensities using Beamline 4B at UVSOR-II. The G.I.[1-10] and G.I.[001] directions imply that the magnetization direction is tilted by 35° toward the surface normal with respect to the given crystal axis direction. The apparent coercivities are found to be larger than ~4 T for both the nanodots and nanowires. The anisotropic magnetic field, which is obtained by the extrapolation of the hard-axis magnetization curve (green lines in Figure 2) up to the saturated magnetization, can be esti-

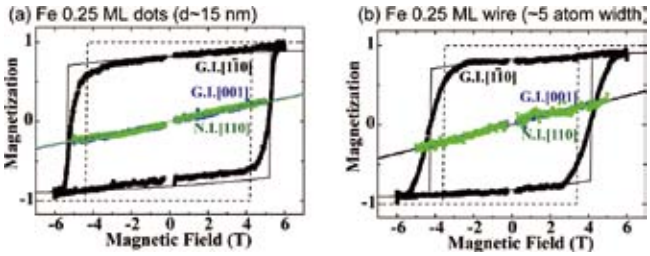


**Figure 2.** Anisotropic magnetization curves of 0.25 ML Fe nanodots (a) and nanowires (b) at 5 K. The data were recorded by measuring the Fe $L_3$-edge circularly polarized X-ray absorption intensities. Huge coercivities along the [1-10] easy axis (black lines) and anisotropic magnetic fields along the hard axes (green) were observed for both nanodots and nanowires.

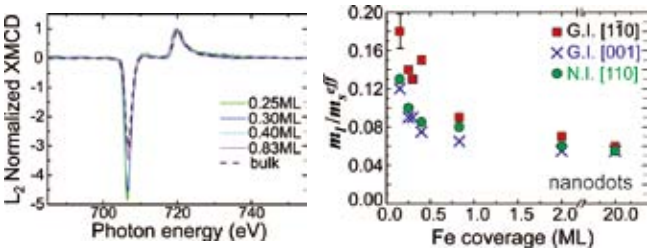


**Figure 3.** (left) Fe $L$-edge XMCD spectra of Fe nanodots on W(110) at 5 K along the G.I.[1-10] axis. (right) Ratio of the orbital magnetic moment ($m_l$) relative to the effective spin magnetic moment ($m_s^{eff}$). Smaller nanodots (lower Fe coverage) show larger orbital magnetic moments.

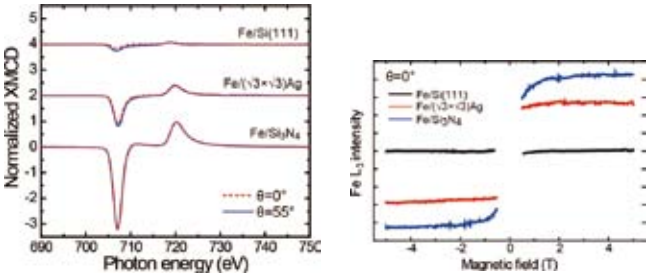


**Figure 4.** (left) Fe $L$-edge XMCD of Fe on clean Si(111) (1.6 ML), Ag/Si(111) (2.0 ML) and $Si_3N_4$ (1.6 ML) at $H$ = ±5 T and $T$ = 5 K. The X-ray incidence angles θ are 0° (normal incidence) and 55° (grazing). (right) Magnetization curves of Fe on clean Si(111) (1.6 ML, black), Ag/Si(111) (2.0 ML, red) and $Si_3N_4$ (1.6 ML, blue), taken at $T$ = 5 K and θ = 0°.

mated to be >15 T. Huge magnetic anisotropy can be concluded both for the nanodots and nanowires. By fitting the experimental data with a simple anisotropic magnetic energy model, the magnetic anisotropic constants were determined to be ~1 meV for both the in-plane and out-of-plane directions, which is a few hundred times larger than that of bulk *bcc* Fe.

Figure 3 shows the Fe $L$-edge XMCD spectra of the nanodots at 5 K. The spectra were normalized with the $L_2$-edge peak tops. As the Fe coverage (nanodot size) decreases, the $L_3$-edge negative peak intensity increases drastically, implying a larger orbital magnetic moment as shown in the right panel of Figure 3. The orbital magnetic moment of the edge Fe atoms may be enhanced.

## 2. Magnetic Properties of Fe Nanostructures on $Si_3N_4$/Si(111)-(8×8) and Ag/Si(111)-(√3×√3)R30°[2)]

The magnetic properties of ferromagnetic transition metals on Si substrates have been widely investigated for the exploitation of new magnetic devices. Since clean Si surfaces react with transition metals very easily to form usually non-magnetic transition-metal silicides, it is essential to insert some inert film between transition metals and Si substrate. No reports have been however published for epitaxially ordered substrates on Si(111). In the present study, we investigated growth processes and magnetic properties of Fe deposited on well-defined $Si_3N_4$/Si(111)-(8×8) and Ag/Si(111)-(√3×√3) R30° by using STM and XMCD.

Figure 4 show the Fe $L$-edge XMCD spectra and the corresponding magnetization curves of Fe deposited on $Si_3N_4$/Si(111)-(8×8), Ag/Si(111)-(√3×√3)R30° and clean Si(111)-(7×7). It is clearly found that the Fe XMCD signals is enhanced in the sequence of Si(111) < Ag/Si(111) < $Si_3N_4$/Si(111). The XMCD sum-rule analysis yields the spin magnetic moments as $m_s$ = 0.17 $\mu_B$ (clean), 1.25 $\mu_B$ (Ag), and 2.62 $\mu_B$ ($Si_3N_4$). On clean Si(111)-(7×7), the spin magnetic moment is almost quenched. On the contrary, Fe/$Si_3N_4$ has a much larger spin magnetic moment, which is even larger than that of *bcc* bulk Fe (2.2 $\mu_B$). Fe/Ag/Si(111) shows a intermediate property. Such a drastic difference among the three substrates is caused by the fact that the $Si_3N_4$ substrate most effectively suppresses the silicide formation. Moreover, it is also found that the magnetic moment of Fe on Ag/Si(111) is lost quite easily by annealing at 500 K ($m_s$ = 0.32 $\mu_B$), while that of Fe on $Si_3N_4$ is sufficiently kept even when the sample is annealed at 500 K ($m_s$ = 2.19 $\mu_B$).

### References

1) T. Nakagawa, Y. Takagi, T. Yokoyama, T. Methfessel, S. Diehl and H.-J. Elmers, *Phys. Rev. B* **86**, 144418 (2012).
2) K. Eguchi, Y. Takagi, T. Nakagawa and T. Yokoyama, *Phys. Rev. B* **85**, 174415 (2012).

* carrying out graduate research on Cooperative Education Program of IMS with Kyoto University

# Design and In-Situ Characterization of Catalyst Surfaces

**Department of Materials Molecular Science**
**Division of Electronic Structure**

| | |
|---|---|
| TADA, Mizuki | Associate Professor |
| MURATSUGU, Satoshi | Assistant Professor |
| MAITY, Niladri | Post-Doctoral Fellow |
| ZHANG, Shenghong | Post-Doctoral Fellow |
| SAIDA, Takahiro | Post-Doctoral Fellow |
| WAKI, Minoru | Post-Doctoral Fellow |
| SODE, Aya | Post-Doctoral Fellow |
| THUMRONGPATANARAKS, Wipavee | JENESYS Program Visiting Scientist |
| GAN, Raymond | Visiting Scientist* |
| JIANG, Lu | Visiting Scientist* |
| LIM, Min Hwee | Visiting Scientist* |
| WANG, Fei | Graduate Student |
| ISHIGURO, Nozomu | Graduate Student† |
| FUNAKI, Yukino | Technical Fellow |
| USUI, Chika | Technical Fellow |
| GONDO, Makiko | Technical Fellow |
| FUKUTOMI, Yukiyo | Secretary |

## 1. Preparation and Catalytic Performances of a Molecularly Imprinted Ru-Complex Catalyst with an $NH_2$ Binding Site on $SiO_2$

The potential of immobilized metal-complex catalysts remarkably interplays with the nature of support surfaces, resulting in significant rate enhancements and unique catalytic performances that their homogeneous counterparts do not exhibit. We proposed the design of molecularly imprinted metal-complex catalysts on $SiO_2$ surfaces, whose ligand was used as a template, and molecularly imprinted metal-complex catalysts have been applied for selective catalysis.

Natural enzymes, which are quite selective catalysts for particular reactants, possess highly sophisticated catalytic systems with active metal species, shape-selective reaction space, and molecular recognition sites spatially arranged for the particular reactants. Artificial design of such a sophisticated catalytic system is still difficult and the preparation of both catalytically active site and shape-selective reaction space with spatially arranged molecular binding sites. We have prepared a molecularly imprinted Ru-complex catalyst with $NH_2$ binding site on the wall of a molecularly imprinted cavity toward the shape-selective transfer hydrogenation catalysis.[1)]

A template alcohol, which was the template for *o*-fluorobenzophenone hydrogenation, was coordinated to a $SiO_2$-supported Ru complex (Ru-*N*-*p*-styrenesulfonyl- 1,2-diphenylethylenediamine) and the hydrolysis polymerization of tetramethoxysilane produced $SiO_2$-matrix overlayers surrounding the supported Ru complex on the surface. A carbamate group (-NHCOO-) connected to a silane-coupling moiety (-Si$(OC_2H_5)_3$) was tethered to the alcohol template and the cleavage of the carbamate moiety after hanging the silane-coupling branch on the wall of a molecularly imprinted cavity produced a spatially arranged $NH_2$ binding site for the hydrogenation of *o*-fluorobenzophenone as shown in Figure 1.

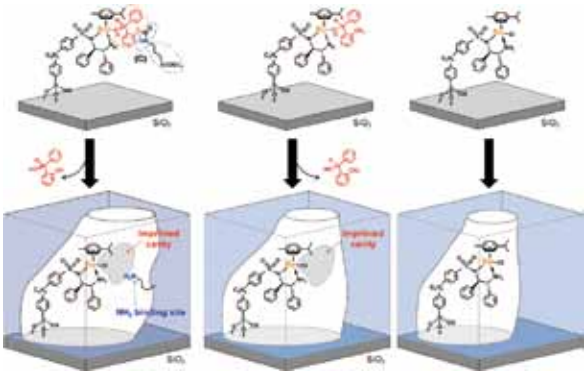

**Figure 1.** Preparation of molecularly imprinted Ru catalysts with an imprinted cavity with an $NH_2$ binding site on the wall of the cavity, with an imprinted cavity without an $NH_2$ binding site, and without an imprinted cavity.

We prepared three catalysts with a molecularly imprinted cavity with an $NH_2$ binding site, with a molecularly imprinted cavity without an $NH_2$ binding site, and without a cavity of the template illustrated in Figure 1. The catalytic performances of the transfer hydrogenation of *o*-fluorobenzophenone were significantly different between these three catalysts under identical reaction conditions. The transfer hydrogenation did not proceed at all on the catalyst prepared without the template. On the other hand, other two catalysts prepared with the templates exhibited activity for the hydrogenation, but we

found differences in the hydrogenation rates of *o*-fluorobenzophenone and *o*-methylbenzophenone. These two reactants have similar shapes to each other, but *o*-fluorobenzophenone with F group, which can interact to the $NH_2$ binding site by hydrogen bonding, was preferably hydrogenated on the molecularly imprinted catalyst with the $NH_2$ binding site. Such differences in the hydrogenation activity were not observed on the imprinted catalyst without the $NH_2$ binding site. The $NH_2$ binding site promoted the preferable adsorption of the specific molecule that can interact with the molecular binding site, resulting in increase in the transfer hydrogenation activity. The strategy is promising to create an artificial enzymatic catalyst surfaces in the future.

## 2. Operando Time-Resolved XAFS for Surface Events on $Pt_3Co$/C and Pt/C Cathode Catalysts in Practical PEFCs during Voltage-Operating Processes

Polymer electrolyte fuel cells (PEFCs) are among the most efficient clean energy technologies, but practical application in automobiles remains challenging because of the high cost and insufficient durability of cathode catalysts. To improve fuel-cell performance and cathode catalyst durability, alloying of Pt with 3*d* transition metal elements is a promising approach. Pt-Co alloy is a representative of the Pt-alloy cathode catalysts and has been reported to be more active and durable than Pt/C catalysts. Although electrochemical surface events have been extensively investigated, the structural kinetics of the transformations of catalyst themselves and the ORR reaction mechanism on practical Pt-Co catalysts have not been established. *In situ* time-resolved QXAFS spectra at the Pt $L_{III}$-edge and Co *K*-edge were measured at 500 ms intervals, and the analysis of the series of the operando QXAFS spectra for the PEFC bimetal cathode catalyst revealed the rate constants of electron transfer, changes in the charge density of $Pt_3Co$ nanoparticles, and changes in the local coordination structures with Pt–Pt, Pt–Co, Co–Co, and Pt–O bonds for the first time (Table 1).[2)]

We compared the reaction mechanism and structural kinetics on the $Pt_3Co$/C and Pt/C catalysts under similar fuel-cell operating conditions. It is to be noted that all the rate constants on the $Pt_3Co$/C catalyst were larger than the corresponding rate constants on the Pt/C catalysts. During the 1.0 V → 0.4 V process, for example, Pt–Pt bond breaking on the $Pt_3Co$/C catalyst was 1.5-fold to that on the Pt/C catalyst. The rate constant of Pt–O bond breaking ($k'_{Pt-O}$), which is highly related to the ORR activity of the cathode catalyst, was about 4 times higher on Pt-Co/C (0.4 $s^{-1}$) than on Pt/C (0.11 $s^{-1}$). There were also a significant difference in the rate constant of Pt–Pt bond re-formation ($k'_{Pt-Pt}$), on $Pt_3Co$/C (0.3 $s^{-1}$) and Pt/C (0.078 $s^{-1}$), which may be relevant for realizing better catalyst durability of the $Pt_3Co$/C catalyst.

The irreversible oxidation of the Pt catalysts depends on the difference in rate between oxidation and reduction of the Pt catalysts during voltage cycling. The repeated cycling on oxidized Pt species which could not be recovered causes extensive dissolution of the Pt cathode catalyst. $Pt_3Co$ alloy systems facilitate reversible oxidation/reduction in the voltage-cycling processes. The structural kinetics determined from the *in situ* time-resolved XAFS revealed that all the rate constants of the surface events on the $Pt_3Co$/C cathode catalyst were higher than those on Pt/C, particularly the reduction steps involving Pt–O bond breaking. Reversible redox cycles on $Pt_3Co$ alloys are suggested as a key factor in the superior performance of $Pt_3Co$ alloy cathode catalysts in PEFCs. Understanding of the fundamental issues of the structural kinetics of the catalyst surface events by *in situ* time-resolved XAFS establishes new boundaries for the regulation and operation of fuel cells.

**Table 1.** Rate constants for $Pt_3Co$/C and Pt/C MEAs in voltage-cycling processes by operando time-resolved XAFS.

| Process | | Rate constant /$s^{-1}$ | |
|---|---|---|---|
| | | $Pt_3Co$/C | Pt/C |
| 0.4 → 1.0 V | XANES white-line height | 0.12 ± 0.02 | 0.073 ± 0.001 |
| | CN (Pt–Pt) | 0.13 ± 0.03 | 0.088 ± 0.008 |
| | CN (Pt–Co) | No change | – |
| | CN (Pt–O) | 0.10 ± 0.03 | 0.076 ± 0.009 |
| | charge in the fuel cell | 2.86 ± 0.04 | 1.84 ± 0.02 |
| | | 0.258 ± 0.003 | 0.167 ± 0.001 |
| 1.0 → 0.4 V | XANES white-line height | 0.24 ± 0.05 | 0.14 ± 0.03 |
| | CN (Pt–Pt) | 0.3 ± 0.1 | 0.078 ± 0.009 |
| | CN (Pt–Co) | No change | – |
| | CN (Pt–O) | 0.4 ± 0.2 | 0.11 ± 0.02 |
| | charge in the fuel cell | 3.68 ± 0.03 | 2.16 ± 0.01 |
| | | 0.484 ± 0.002 | 0.259 ± 0.001 |

### References

1) Y. Yang, Z. Weng, S. Muratsugu, N. Ishiguro, S. Ohkoshi and M. Tada, *Chem. –Eur. J.* **18**, 1142–1153 (2012).
2) N. Ishiguro, T. Saida, T. Uruga, O. Sekizawa, S. Nagamatsu, K. Nitta, T. Yamamoto, S. Ohkoshi, Y. Iwasawa, T. Yokoyama and M. Tada, *ACS Catal.* **2**, 1319–1330 (2012).

### Award

ISHIGURO, Nozomu; Student Presentation Award (JXAFS 14).

* IMS International Collaboration Program

† carrying out graduate research on Cooperative Education Program of IMS with The University of Tokyo

# Studies of Field-Effect-Transistor Based on Highly-Correlated Molecular Materials

**Department of Materials Molecular Science**
**Division of Electronic Properties**

YAMAMOTO, Hiroshi — Professor (April, 2012–)
URUICHI, Mikio — Technical Associate
SHIMIZU, Atsuko — Secretary

Field effect transistor (FET) with organic molecules as a channel material is under intense studies because of its application possibilities such as flexible, printable, and large-area electronic devices. Despite such a thorough investigation on single-component neutral molecules to pursuit high performance (say, high mobility *etc*.) in FET uses, few studies are known for compound organic semiconductor- based transistors. We have been exploiting FET devices with charged molecular materials, namely cation-radical salts of electron-donating molecules (donors) such as BEDT-TTF and anion-radical salts of electron accepting molecules (acceptors) such as $Ni(dmit)_2$. Among these materials, our focus concentrates in Mott-insulators in which Coulomb interaction among carriers blocks metallic transport. In this highly correlated situation of charge carriers, Mott insulator stays in a fragile semiconducting state, where carrier injection, chemical and/or physical pressure (or strain), and thermal fluctuation can drive it into a metallic state by phase transition (*i.e.* Mott transition: Figure 1). Since the carrier density (band-filling) of a FET interface can be finely modulated by an electrostatic field from the gate electrode, it is anticipated that the Mott-insulating state can be switched to a metallic state by a field effect. Indeed, our previous work showed such an insulator-to-metal transition in terms of the band structure, and these results provide not only a possibility of application use of organic Mott-FET but also a significant insight into the mechanism of Mott transition itself. We are now expanding our research target both to the superconducting transition of Mott-FET and to its room-temperature operation.
(BEDT-TTF = bis(ethylenedithio)tetrathiafulvalene,
dmit = 1,3-dithiole-2-thione-4,5-dithiolate)

## 1. Field-Induced Superconductivity in an Organic Mott-FET

κ-(BEDT-TTF)$Cu[N(CN)_2]Br$ (κ-Br) is an organic superconductor whose electronic state is Mott-insulating at room-temperature but turns into metallic at low temperature through a crossover around 50–100 K, possibly because of an increase of bandwidth upon thermal contraction. In our previous works, a tensile strain altered its ground state into a Mott-insulating state, when its thin (100–300 nm) crystal is laminated on top of $SiO_2/Si^{++}$ substrate and cooled down to low temperature.

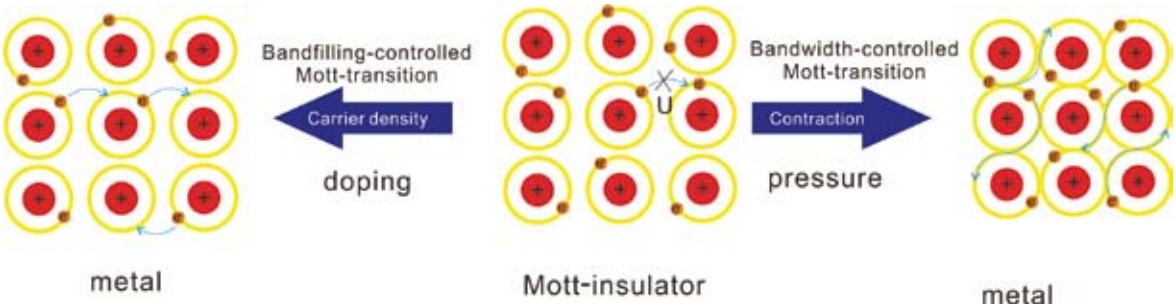


**Figure 1**. Concept of a Mott-insulator (center) along with its bandfilling-controlled (left) and bandwidth-controlled (right) Mott transitions. When the band is half-filled and band energy is small, the carriers are localized because of on-site Coulomb interaction (*U*). This situation is broken down either by changing the carrier concentration or by compressing the lattice. In many cases, the Mott transitions are associated with superconductivity at the boundary between metallic and insulating phases.

Although the electronic state at low temperature became completely insulating in this experiment because of the very small thermal expansion coefficient of Si substrate (2 ppm/K), one can anticipate from the *T–P* (temperature *vs.* pressure) phase diagram that somehow mixed electronic state between superconducting and Mott-insulating states can be realized when the tensile strain is much weaker. To achieve such a mixed state in the device, where phase-separation occurs between superconducting and Mott-insulating states, we have chosen Nb-doped $SrTiO_3$ as a back-gate substrate because of its larger thermal expansion coefficient (*ca.* 10 ppm/K) than Si. An aluminum oxide layer was grown by atomic layer deposition technique to form a gate dielectric on the substrate. After lamination process of κ-Br on the substrate, the Mott-FET device which showed a weakly insulating behavior at low temperature was fabricated (Figure 2). Upon applying a positive gate voltage, however, the resistivity goes down and weakly metallic behavior was observed at $V_G > 2$ V. By further increasing the gate voltage up to 8 V, the device showed a sudden drop of resistivity around 5 K, which can be attributed to superconductivity. Taking account of bistable IV characteristics observed in the low resistance region, the above transition can be understood as a percolation transition of superconducting islands that is induced by the electrostatic doping of electrons. The transition temperature increases as the gate voltage rises and saturates around $V_G = 11$ V. The above result is the first example of field-induced superconductivity in organic materials, and can be utilized for uncovering a phase diagram of organic Mott system in the band filling controlled regime.

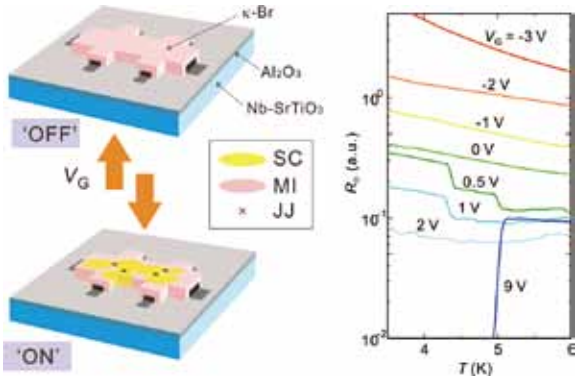


**Figure 2.** The device structure and temperature dependency of device resistance under various gate voltages. The device comprises κ-Br thin-layer single crystal and $Al_2O_3/SrTiO_3$ substrate. By applying a positive gate voltage, the resistance of the device starts decreasing, while a negative gate voltage results in an increase of the resistance. Although superconducting (SC) and Mott-insulating (MI) phases are separated in the device, the four-terminal resistance drops to zero when the Josephson junction (JJ) network forms a pathway to shunt the voltage terminals. This kind of percolation transition is clearly observed in the right panel, where the resistance drops at 5 K with a gate voltage of 9 V.

## 2. Operation of Organic Mott-FET at Higher Temperature

In order to operate the organic Mott-FET at higher temperature, hopefully at room temperature, it is necessary to realize much larger Mott gap energy and thinner crystal thickness. For this purpose, we are examining several strategies in parallel.

κ-(BEDT-TTF)Cu[$N(CN)_2$]Cl (κ-Cl) is a Mott-insulator with larger Mott gap than κ-Br and is therefore suitable for examining the influence of an increase in Mott-gap energy on the device performance. For example, it has higher resistance than κ-Br and exhibit better ON/OFF ratio. In addition, it always shows ambipolar behavior, probably because of its clean surface (Figure 3). This situation allows us to analyze the critical exponents of filling-controlled Mott transition, which will give us important information about ON/OFF efficiency of the device. Because it is also possible to control the Mott gap energy by applying a mechanical strain, κ-Cl device provides an ideal platform to expand Mott-FET strategy to higher temperature.

Another candidate of the channel material for Mott-FET that can be used at room temperature is (BEDT-TTF)(TCNQ). We are exploiting this material both in a crystalline and amorphous form to find a better FET setup for simple but highly efficient device at room temperature. (TCNQ = tetracyanoquinonedimethane)

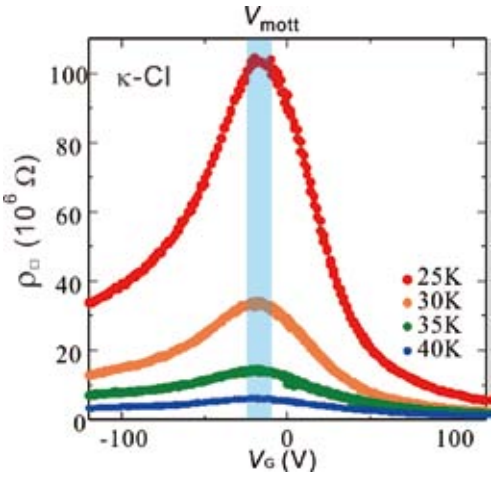


**Figure 3**. Gate voltage dependence of the resistance for κ-Cl based Mott-FET. Because this device clearly shows ambipolar behavior due to a smaller number of mid-gap trap states, it is possible to exactly define the gate voltage for charge neutrality point ($V_{Mott}$). This fact helps determining the critical exponent for Mott transition, which is important both for theoretical investigation and for analyzing device parameters such as subthreshold swing.

### Reference

1) Y. Kawasugi, H. M. Yamamoto, N. Tajima, T. Fukunaga, K. Tsukagoshi and R. Kato, *Phys. Rev. B* **84**, 125129 (9 pages) (2011).

# Magnetic Resonance Studies for Molecular-Based Conductors

**Department of Materials Molecular Science**
**Division of Electronic Properties**

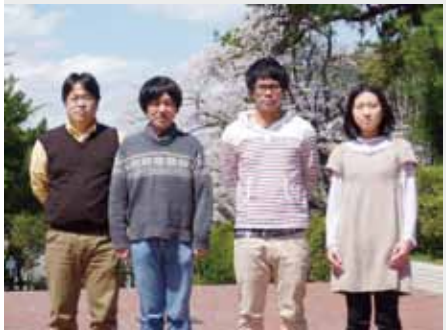

| | |
|---|---|
| NAKAMURA, Toshikazu | Associate Professor |
| FURUKAWA, Ko | Assistant Professor |
| TAKAHASHI, Seiya | Graduate Student* |
| ABE, Hitomi | Secretary |


Magnetic resonance measurements are advantageous for studying fundamental electronic properties and for understanding the detailed electronic structures of molecular based compounds. Developing an understanding of the electronic phases and functionality of these materials enables us to perform systematic investigations of low-dimensional, highly-correlated electron systems and functional materials. Competition between the electronic phases in molecular-based conductors has attracted much attention. The investigations of such electronic phases by magnetic resonance measurements are important to understanding unsolved fundamental problems in the field of solid state physics, and to explore novel functionalities in the field of material science.

In this study, we performed broad-line NMR and ESR measurements on molecular-based conductors to understand electron spin dynamics and functionality in low-temperature electronic phases.

## 1. $^{13}$C NMR Study of the Magnetic Properties of the Quasi-One-Dimensional Conductor, $(TMTTF)_2SbF_6$

Magnetic properties in the quasi-one-dimensional organic salt, $(TMTTF)_2SbF_6$, where TMTTF is tetramethyltetrathiafulvalene, are investigated by $^{13}$C NMR under pressures. Antiferromagnetic phase transition at ambient pressure (AFI) is confirmed. Charge ordering is suppressed by pressure and is not observed under 8 kbar. For $5 < P < 20$ kbar, a sharp spectrum and the rapid decrease of the spin-lattice relaxation rate $1/T_1$ were observed below about 4 K, which is attributed to a spin-gap transition. Above 20 kbar, an extremely broadened spectrum and a critical increase of $1/T_1$ were observed. This indicates that the system enters into another antiferromagnetic phase (AFII) under pressure. The slope of the antiferromagnetic phase transition temperature $T_{AFII}$, $dT_{AFII}/dP$, is positive, while $T_{AFI}$ decreases with pressure. The magnetic moment is weakly incommensurate with the lattice at 30 kbar.

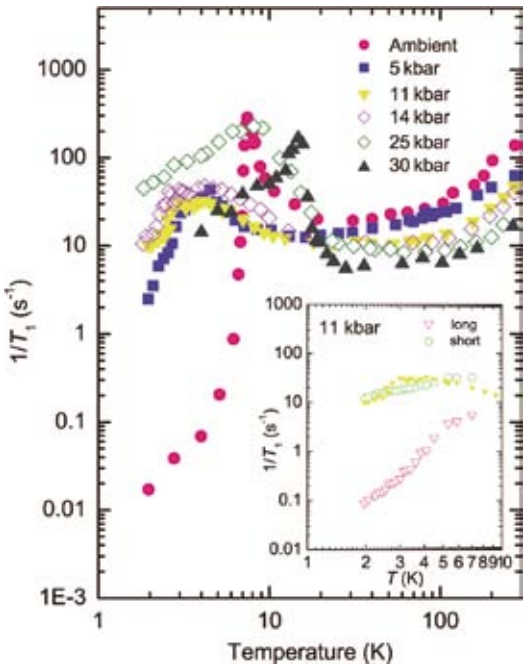


**Figure 1**. Temperature dependence of the $^{13}$C-NMR spin-lattice relaxation rate, $1/T_1$, at six different pressures.

## 2. Time-Resolved ESR Study for Photoconductive Mechanism of Photoconductive TTF-Derivatives

The spin dynamics of photoconductive ethylene-dithiolo-tetrathiafulvalene (EDT-TTF) containing 1,3-benzothiazole (BTA) was examined for froze solution and powdered samples using time-resolved electron spin resonance (TR-ESR) spectroscopy. While the TR-ESR signal of a frozen solution sample under visible excitation were attributed to the excited triplet state $\mathbf{T_1}$, that of the powdered indicates a charge-separated state. It is a characteristic feature of molecular assembled system.

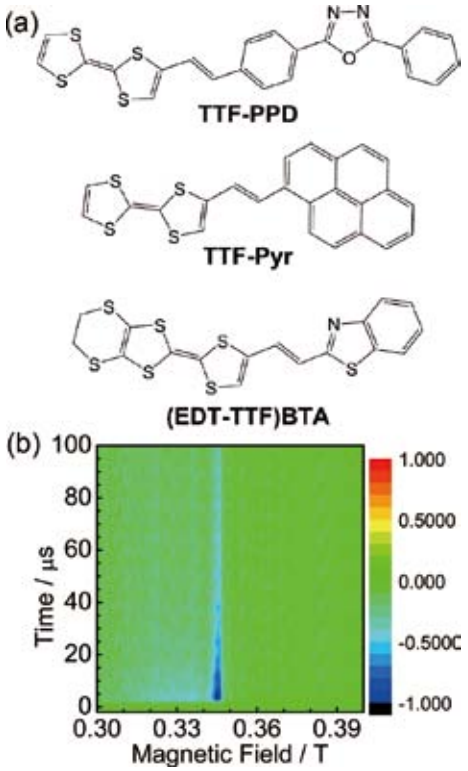


**Figure 2.** (a) Molecular structure of single-molecule-type photoconductive materials, TTF and EDT-TTF derivatives. (b) 2D pulsed TR-ESR spectra for powder sample of photoconductive EDT-TTF containing BTA. The normal axis represents the ESR signal intensity. The color scale denotes the signal intensity. Positive and negative values indicate the absorption and emission of microwaves, respectively.

## 3. Physical Properties of a Molecular Conductor $(BEDT\text{-}TTF)_2I_3$ Nanohybridized with Silica Nanoparticles by Dry Grinding

The dry grinding of a mixture of bis(ethylenedithio)tetrathiafulvalene (BEDT-TTF) and silica nanoparticles has produced powdery (BEDT-TTF)–silica nanocomposites. The (BEDT-TTF)–silica nanocomposites are readily doped with iodine in hexane dispersion to give powdery nanocomposites of $(BEDT\text{-}TTF)_2I_3$–silica. XRD and TEM measurements suggest that $(BEDT\text{-}TTF)_2I_3$ in the nanocomposite exists as shell layers of core-shell-type nanoparticles and as nanometre-sized crystals incorporated into hollow sites of aggregated silica nanoparticles. Magnetic susceptibility measurements reveal that the nanocomposites accompanied a large number of Curie spins attributable to surface molecules of the core-shell-type nanoparticles. The nanocomposites show a magnetic susceptibility change corresponding to the metal–insulator transition of α-$(BEDT\text{-}TTF)_2I_3$ in a broad temperature range of 110–140 K, which is attributed to the properties of the nanocrystalline components. Doping in diethyl ether dispersion leads to higher amounts of the nanocrystalline component being obtained. The doping of (BEDT-TTF)–silica nanocomposites by dry grinding produces a paramagnetic powder containing amorphous $(BEDT\text{-}TTF)_2I_3$, which possesses a Curie spin concentration of 50%. The effects of annealing on these nanocomposites are investigated. The electrical conductivity of the compaction pellets of (BEDT-TTF)–silica nanocomposites is enhanced by iodine doping to reach approximately $10^{-6}$ S $cm^{-1}$, but the value is much lower than that of the bulk crystals ($10^1$ S $cm^{-1}$).

## 4. Electronic Properties and $^1H$ Dynamics in Self-Doped Organic Conductor $(TTFCOO)[(NH_4^{+1})_{1-x}(NH_3)_x]$

$^1H$-NMR and High-Field ESR measurements were carried out for self-doped type organic conductor, $(TTFCOO)[(NH_4^{+1})_{1-x}(NH_3)_x]$ and its deuterated salt. $(TTFCOO)[(NH_4^{+1})_{1-x}(NH_3)_x]$ and related salts are TTF-based self-doped hydrogen-bonding conductor developed by NIMS group. The TTF-skeleton stacks to form a one-dimensional column. The pristine $TTFCOONH_4$ molecule is closed-shell. Self-doped type carrier is generated by substitution of the end group of ($NH_3^0$) with ($NH_4^{+1}$), which is regarded as a charge-reservoir. Actually, a considerable concentration of $NH_3$ molecules has been confirmed by X-ray photoelectron spectroscopy data. According to the static magnetic susceptibility and high-field ESR measurements, we found that the observed spin was distributed on quasi-hole-like TTF skeletons, and that the TTFCOO mainframe partially becomes a neutral radical. The spin susceptibility was well fitted with a Curie-Weiss term and an activation-type term. The activation-type term was dominant at high temperatures.

In order to clarify the $^1H$ dynamics, we carried out $^1H$-NMR measurements for pristine and deuterated salts. The $^1H$-NMR spin-lattice relaxation rate, $^1H$-$T_1^{-1}$, of indicates a characteristic temperature and frequency dependence. A pronounced peak observed at around 200 K is possibly due to molecular motion. Since the relaxation curve is not single component below 200 K, we assumed the $^1H$-$T_1^{-1}$ from initial slope (weighted average). Below 100 K $^1H$-$T_1^{-1}$ follows $T^{0.5}$, and remains frequency dependence, indicating a 1D spin-diffusion type relaxation. However, the Fermi surface of $(TTFCOO)[(NH_4^{+1})_{1-x}(NH_3)_x]$ is considered to be 2D, according to the tight-binding band calculation. This discrepancy is an open question at present.

### References

1) F. Iwase, K. Sugiura, K. Furukawa and T. Nakamura, *Phys. Rev. B* **84**, 115140 (7 pages) (2011).
2) K. Furukawa, Y. Sugishima, H. Fujiwara and T. Nakamura, *Chem. Lett.* **40**, 292–294 (2011).
3) A. Funabiki, H. Sugiyama, T. Mochida, K. Ichimura, T. Okubo, K. Furukawa and T. Nakamura, *RSC Adv.* **2**, 1055–1060 (2012).

* carrying out graduate research on Cooperative Education Program of IMS with Yokohama National University

# Design of Porous Polymer Frameworks

**Department of Materials Molecular Science**
**Division of Molecular Functions**

| | |
|---|---|
| JIANG, Donglin | Associate Professor |
| NAGAI, Atsushi | Assistant Professor |
| LIU, Xiaoming | Post-Doctoral Fellow |
| GUO, Zhaoqi | Post-Doctoral Fellow |
| LIN, Jianbin | Post-Doctoral Fellow |
| XU, Yanhong | Graduate Student |
| DING, Xuesong | Graduate Student |
| JIN, Shangbin | Graduate Student |
| CHEN, Xiong | Graduate Student |
| FENG, Xiao | Graduate Student |
| CHEN, Long | Graduate Student |
| XU, Hong | Graduate Student |
| WU, Yang | Graduate Student |
| SUZUKI, Hiroko | Secretary |


Covalent organic frameworks (COFs) are crystalline porous polymers that allow organizaiton of organic units into long-range-ordered two and three-dimensional periodicities.[1)] COFs are intriguing frameworks because they allow a new degree of control of porosity, composition and component positions. In our group, we have pioneered the synthesis of π-electronic 2D COFs with various π-units.[1–6)]

Conjugated microporous polymers (CMPs) are a class of porous organic frameworks consisting of extended π-conjugation and inherent nanopores. The π-conjugation skeletons together with the well-defined nanopores enable the development of novel materials that are completely different from traditional linear conjugated polymers and conventional porous polymeric materials lacking of strong π correlations among the building blocks. We have developed CMPs as a new platform to achieve light-emitting, light-harvesting, catalysis, energy storage, and sensing functions.[7,8)]

## 1. Pore Surface Engineering of COFs

COFs are a class of important porous materials that enable pre-designable pore size and geometry; however, pore surface engineering in COFs remains challenging. COFs, which offers precise control over the composition, density, and functionalities of organic groups anchored onto the pore walls.[2)] For this purpose, an azide-appended phenylene block was synthesized and utilized as the wall component in a two-component condensation system for the construction of COFs with azide-integrated walls. The two-component system was further developed to a three-component system that consists of azide-appended phenylene and 'naked' phenylene walls, and corner blocks, thereby enabling the synthesis of COFs bearing a tunable content of azide units on the walls. The azide units on the COF walls were found to undergo quantitative click reaction with alkynes to form triazole-linked groups on the wall surfaces. Consequently, the combination of a three-component condensation system with click reaction led to the establishment of a protocol that allowed control of both the composition and density of organic groups in the pores (Figure 1). This methodology was widely useful for the creation of various specific surfaces in COF pores.[2)]

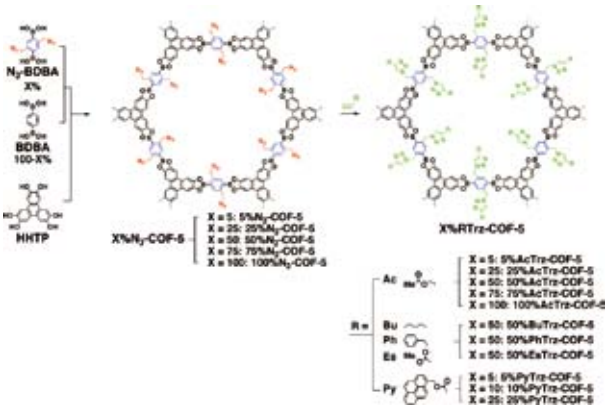


**Figure 1.** A general strategy for the surface engineering of COFs through the combination of condensation reaction and click chemistry. COFs bearing azide units on the walls are synthesized by the condensation reaction of hexahydroxytriphenylene (HHTP) with azide-appended benzene diboronic acid ($N_3$-BDBA) and benzene diboronic acid (BDBA) in a designated molar ratio ($X$ = 0–100%). The azide groups on the COF walls are clicked with alkynes to anchor various organic groups onto the walls of COFs ($X$%RTrz-COF-5). The density of R surface groups on the walls is determined by the azide content in $X$%$N_3$-COF-5.

COF-5 is a typical mesoporous COF that consists of triphenylene at the corners and phenylene on the walls of a boronate ester-linked 2D hexagonal skeleton.1 We introduced azide groups to the 2 and 5 positions of the phenylene unit of 1,4-benzenediboronic acid and utilized the azide-appended benzenediboronic acid ($N_3$-BDBA) as wall blocks for the condensation reaction with hexahydroxytriphenylene (HHTP) (Figure 1). The resulting hexagonal skeleton is identical to that of COF-5, with triphenylene corners but azide-appended phenylene walls. Such a strategy allows the growth of various specific groups on the surface because the azide units in the

skeletons are reactive groups that can click with various alkynes for pre-designable functionalization. The content of azide units on the pore walls can be tuned using a three-component condensation system using HHTP as the corners and a mixture of $N_3$-BDAB and BDBA as the walls, because the azide units in $N_3$-BDAB did not affect the reactivity of BDBA in the condensation.

Azide units are well established for click reactions with alkynes to introduce functional groups via 1,2,3-triazole rings (Trz). Reaction of azide units on the walls of *X*%$N_3$-COF-5 (*X* = 5, 25, 50, 75, and 100) in a typical click reaction with 2-propynyl acetate in anhydrous N,N-dimethylacetamide (DMAc) at 50 °C with CuI present as a catalyst gives the corresponding *X*%AcTrz-COF-5 in quantitative yields. The present strategy can be further extended to the introduction of various specific groups onto the walls of COFs. We selected a paraffinic unit, aromatic hydrocarbon, and ester groups as typical examples to react with 50%$N_3$-COF-5. The click reactions of 50%$N_3$-COF-5 with 1-hexyne, 3-phenyl-1-propyne, and methyl propiolate were quantitatively achieved and led to the integration of *n*-butyl, benzyl, and methyl ester units to the walls of COF-5.

The present method for the pore surface engineering of COFs is simple and universal. This approach is high throughput due to the high efficiency condensation reaction and the quantitative click reaction. The most significant feature is that the combination of condensation and click reactions enables the molecular design of pore surface with controlled composition, component, and density. Therefore, this approach provides a new aspect in the chemistry of these well-defined porous materials, and provides a means to tailor pores for specific purposes and applications.

## 2. Highly Luminescent CMPs with Facilitated Exciton Migration and Improved Light-Emitting Activity

Conjugated polymers play a vital role in lasing, light-emitting diodes, flexible transistors, and solar cells. Owing to their rigid conformation, they have a high tendency to aggregate in solution and the solid state. Such aggregation leads to the dissipation of excitation energy and ultimately limits their utility as light-emitting motifs.

Herein we report a new strategy for the construction of light-emitting conjugated polymers based on conjugated microporous architectures.[7] We have developed a highly luminescent CMP with tetrakisphenylethene(TPE) as building block (Figure 2, TPE-CMP). Owing to the crosslinking nature of CMP, TPE-CMP can suppress the rotation of TPE units, thus allowing the high luminescence in both solution and solid states. As a result, a positive "CMP effect" was observed, *i.e.* the interweaving CMP architecture can promote π conjugation, facilitates excitation migration, and improves luminescence activity. Changing the reaction time allows for the synthesis of a series of CMPs with different size and absorption band. As the reaction time increased, the TPE-CMP particles become larger to give an increased surface area and display red-shifted electronic absorption band accordingly.

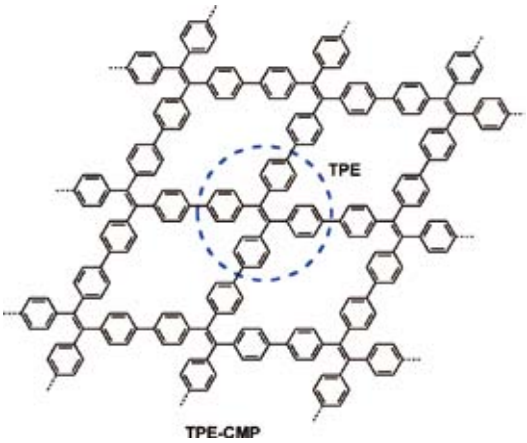


**Figure 2.** Structure of TPE-CMP.

These results the propagation of network structure takes place with the reaction time. The fluorescence quantum yield could reach 40%. In contrast, linear TPE polymer showed a low quantum yield of only 0.65% at otherwise identical condition. Interesting, owing to the crosslinking nature of the network, TPE-CMP is highly luminescent in various solvents such as methanol, dioxane, tetrohydorfuran, dichloromethane, chloroform, hexane, dimethylforamide, benzene, and water while the linear polymer analogue is almost nonemissive in solvents such as dichloromethane, chloroform, and tetrehydrofuran. Furthermore, TPE-CMP emits strong luminescence at solid state with a similar emission band as that in solutions. Fluorescence anisotropy measurements suggest that the exciton can migrate over the three-dimensional CMP skeletons. These positive CMP effects suggest that the CMP architecture provides a new platform for the design of highly luminescent materials

### References

1) X. Feng, X. Ding and D. Jiang, *Chem. Soc. Rev.* **41**, 6102 (2012).
2) A. Nagai, Z. Guo, X. Feng, S. Jin, X. Chen, X. Ding and D. Jiang, *Nat. Commun.* 2:536 doi: 10.1038/ncomms1542 (2011).
3) X. Ding, X. Feng, A. Saeki, S. Seki, A. Nagai and D. Jiang, *Chem. Commun.* **48**, 8952–8954 (2012).
4) X. Feng, L. Chen, Y. Honsho, O. Saengsawang, L. Liu, L. Wang, A. Saeki, S. Irle, S. Seki, Y. Dong and D. Jiang, *Adv. Mater.* **24**, 3026–3031 (2012).
5) X. Feng, L. Liu, Y. Honsho, A. Saeki, S. Seki, S. Irle, Y. Dong, A. Nagai and D. Jiang, *Angew. Chem., Int. Ed.* **51**, 2618–2622 (2012).
6) X. Ding, L. Chen, Y. Honsho, X. Feng, O. Saengsawang, J. Guo, A. Saeki, S. Seki, S. Irle, S. Nagase, P. Vudhichai and D. Jiang, *J. Am. Chem. Soc.* **133**, 14510–14513 (2011).
7) Y. Xu, L. Chen, Z. Guo, A. Nagai and D. Jiang, *J. Am. Chem. Soc.* **133**, 17622–17625 (2011).
8) X. Liu, Y. Xu and D. Jiang, *J. Am. Chem. Soc.* **134**, 8738–8742 (2012).

# Solid State NMR for Molecular Science

**Department of Materials Molecular Science**
**Division of Molecular Functions**

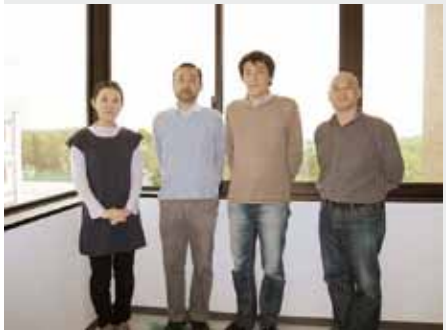

NISHIMURA, Katsuyuki — Associate Professor
IIJIMA, Takahiro — Assistant Professor
TANIO, Michikazu — IMS Research Assistant Professor

We are working on methodology and hardware developments of solid state NMR and structural biology and materials molecular science. In the following, we show studies of peripheral membrane proteins and inorganic compounds based on NMR.

## 1. NMR and Native-PAGE Analyses of the Phospholipase C-δ1 Pleckstrin Homology Domain

Phospholipase C (PLC) binds to phosphatidylinositol 4,5-bisphosphate ($PIP_2$) in the cell membrane through the pleckstrin homology (PH) domain, and hydrolyzes $PIP_2$ to produce two second messengers, diacylglycerol and inositol 1,4,5-triphosphate ($IP_3$), by the catalytic domain. The PLC-δ1 PH domain has a characteristic short α-helix (α2) from residues 82-87 (Figure 1). Solid-state $^{13}C$ NMR studies of the PLC-δ1 PH domain suggested that the α2-helix non-specifically interacts with the hydrophobic layer of the membrane due to the membrane localization of the protein.[1)]

In this study, the contributions of the α2-helix toward the $IP_3$ binding activity and thermal stability of the PLC-δ1 PH domain were therefore investigated by using NMR and Native-PAGE methods.

Native-PAGE analyses indicated that $IP_3$ binding to the PLC-δ1 PH domain results in a drastic migration shift on the gel and in an increased thermal stability. In addition, we found that disruption of the α-helical conformation by replacement of Lys-86 with proline resulted in reduced affinity for $IP_3$ and in thermal destabilization of the $IP_3$-binding state. Although the mutant protein with replacement of Lys-86 with alanine showed a slight reduction in thermal stability, the $IP_3$-binding affinity was similar to that of the wild-type protein. Replacement of Phe-87 with alanine, but not with tyrosine, also resulted in reduced affinity for $IP_3$ and in thermal instability. These results indicated that the helical conformation of the α2-helix and the phenyl ring of Phe-87 play important roles in the $IP_3$-binding activity and thermal stability of the PLC-δ1 PH domain.[2)] The $^{1}H$-$^{15}N$ HSQC NMR study of the selectively [α-$^{15}N$]Lys-labeled PLC-δ1 PH domain indicated that

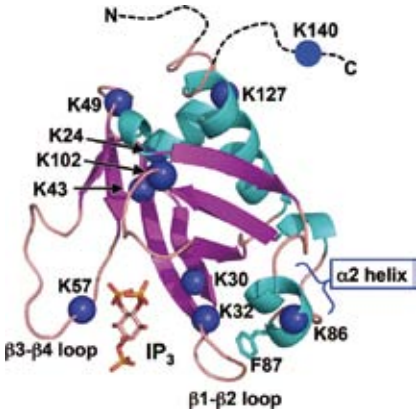


**Figure 1.** Crystal structure of the PLC-δ1 PH domain complexed with $IP_3$ (PDB ID, 1MAI).

$IP_3$ binding induces chemical shift displacement of all lysine signals (Figure 2). Interestingly, among those signals, only line width of α-$^{15}N$ signal from Lys-86 located on the α2-helix markedly changed due to $IP_3$ binding (Figure 2, inset): in the ligand-free form, the α-$^{15}N$ signal line width of Lys-86 was about two-fold broader than those of the other lysine signals in the one-dimensional $^{15}N$ projection of the $^{1}H$-$^{15}N$ HSQC NMR spectrum, and the addition of $IP_3$ resulted in line narrowing, and that the broad line width of the [α-$^{15}N$]Lys-86 signal converts to a narrow line width with addition of $IP_3$ (Figure 2). These findings provide evidence that the conformation and/or dynamics of the α2-helix couple with the ligand-binding activity of the PLC-δ1 PH domain. These findings suggested that the conformational changes of the α2-helix induced by membrane binding result in conversion of the stereospecific ligand-binding site to a weak-affinity site and in protein instability. Based on these results, we propose a new affinity regulation mechanism in which the ligand stereospecificity of the PLC-δ1 PH domain is significantly reduced due to protein structural changes by the membrane binding, and non-specific membrane binding or insertion is therefore important for stable anchoring to the lipid membrane. These findings also suggest that the ligand stereospecificity of the protein mainly contributes to searching the membrane contain-

ing $PIP_2$ and that stable anchoring to the lipid membrane is mainly achieved by non-specific membrane binding or insertion rather than $PIP_2$ binding. This mechanism also explains the lower affinity of the protein to lipid bilayers than $IP_3$, which is an essential property for feedback control of catalytic reaction of PLC-δ1 with respect to $PIP_2$.

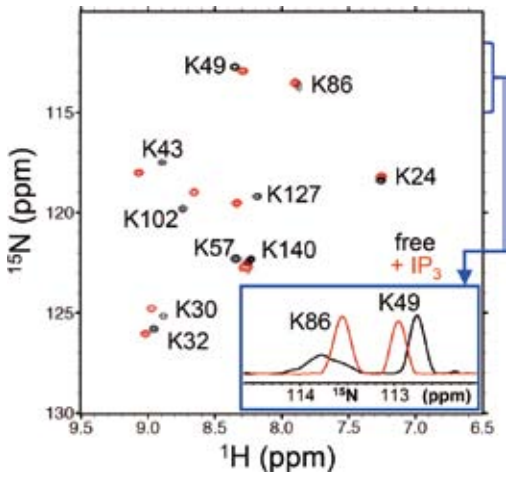


**Figure 2.** Solution NMR analyses of the [α-$^{15}$N]Lys-labeled PLC-δ1 PH domain. The $^{1}$H-$^{15}$N HSQC NMR spectra without (black) and with (red) $IP_3$. (inset) The one-dimensional $^{15}$N projections of the HSQC NMR spectra around the Lys-86 signal under the absence (black) and presence (red) of $IP_3$.

## 2. Solid State $^{95}$Mo NMR of Paramagnetic Crystals of Polyoxomolybdates

For a group 6 element of molybdenum, there exist stable compounds with all valences from Mo(0) to Mo(VI). Among them, Mo(V) species are included in materials such as ε-Keggin anion and nanosized oxides with ring-, tube- and ball-structure. Localization of the $d^1$ electron in Mo(V) has attracted attention in terms of molecular design and solid state physics like optic, electric and magnetic properties. Since $^{95}$Mo is a quadrupole nuclei of spin $I = 5/2$ with the small gyromagnetic ratio $\gamma = -1.743 \times 10^7$ rad $s^{-1}$ $T^{-1}$, it is difficult to measure $^{95}$Mo NMR spectra in solid state in general. Recently, we have reported solid-state $^{95}$Mo NMR spectra of mixed balanced polyoxomolybdates(V, VI) with the localized or delocalized $d^1$ electrons measured by enhancing sensitivity and resolution using a high-field magnet.[3] Furthermore, we clarified a disorder structure of $[PMo_{12}O_{36}(OH)_4\{La(H_2O)_{2.75}Cl_{1.25}\}_4]27H_2O$ with the ε-Keggin $\{Mo_{12}\}$ core by $^{95}$Mo NMR in solids.

In this study, we investigated a paramagnetic polyoxomolybdate of $[Mo_{12}O_{30}(OH)_{10}H_2\{Ni(H_2O)_3\}_4]$ (hereafter, abbreviated as $\{Mo_{12}\}(Ni)$). Although the core of this crystal is also ε-Keggin $\{Mo_{12}\}$, it is caped with four paramagnetic $Ni(II)(H_2O)_3$. In order to examine coupling constants appearing in solid state NMR, we measured high-field $^{95}$Mo NMR in solids, simulated the obtained spectra numerically, and performed DFT calculation.

Figures 3(i-a) and 3(ii-a) show the $^{95}$Mo NMR static spectra of $\{Mo_{12}\}(Ni)$ measured under 21.8 and 11.7 T, respectively. Considerably broadened spectra with breadth of several thousands of ppm were obtained under both magnetic fields. In the spectral simulation, in addition to the quadrupole and chemical shift interactions, the hyperfine interaction between $^{95}$Mo nuclei and unpaired electron spins in paramagnetic Ni(II) ions were considered as internal interactions. The simulated spectra shown in Figures 3(ii-a) and 3(ii-b) represented experimental spectra well. Since the broadening due to the quadrupole and anisotropic chemical shift interactions were quite large, the effect of the anisotropic hyperfine interaction on the spectral lineshape was small. In order to investigate the contribution from the isotropic hyperfine interaction, the $^{95}$Mo NMR spectrum was measured at 173 K under 11.7 T (Figure 3(i-c)). Notable difference of the spectra between 301 and 173 K was not found. By lowering of temperature, although the line width was slightly broadened owing to the increase of magnetization of the electron spins, we needed not consider temperature dependence of the isotropic shift in the simulation.

The coupling constants for the internal spin interactions were also obtained from DFT calculation. Although the chemical shift estimated by DFT was larger than that by the spectral simulation, the trend such as a considerably large anisotropic chemical shift agreed between DFT and spectral simulation. Also, a spin density localized around the Ni(II) ions was obtained by DFT calculation, which agreed with small temperature-dependence of the whole shift of the spectra.

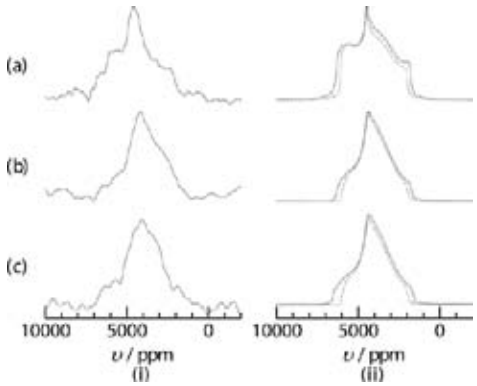


**Figure 3.** $^{95}$Mo NMR static spectra of $\{Mo_{12}\}(Ni)$ under the magnetic field of (a) 21.8 and (b, c) 11.7 T. (b) and (c) show the spectra at 301 and 173 K, respectively. (i) and (ii) show the observed and simulated spectra, respectively. The solid and broken lines in (ii) show the theoretical curves with and without considering the hyperfine interaction, respectively.

### References

1) N. Uekama, T. Aoki, T. Maruoka, S. Kurisu, A. Hatakeyama, S. Yamaguchi, M. Okada, H. Yagisawa, K. Nishimura and S. Tuzi, *Biochim. Biophys. Acta* **1788**, 2575–258 (2009).
2) M.Tanio and K.Nishimura, *Anal. Biochem.* **431**, 106–114 (2012).
3) T. Iijima, T. Yamase, M. Tansho, T. Shimizu and K. Nishimura, *Chem. Phys. Lett.* **487**, 232–236 (2010).

# Organic Solar Cells

**Research Center for Molecular Scale Nanoscience**
**Division of Molecular Nanoscience**

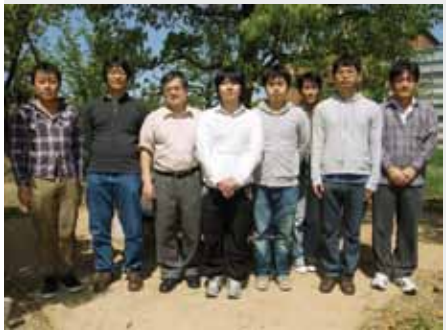

| | |
|---|---|
| HIRAMOTO, Masahiro | Professor |
| KAJI, Toshihiko | Assistant Professor |
| NAKAO, Satoru | Post-Doctoral Fellow |
| SHINMURA, Yusuke | Research Fellow |
| KUBO, Masayuki | Research Fellow |
| YOKOYAMA, Kazuya | Research Fellow |
| YOSHIOKA, Tadashi | Research Fellow |
| ISHIYAMA, Norihiro | Graduate Student |
| SUGIHARA, Hidemi | Secretary |


Organic solar cell is recognized as a next generation solar cell. In 2009, we started CREST Project; "Bandgap Science for Organic Solar Cells." Target of this project is 15% efficiency of organic solar cells by establishing bandgap science for organic semiconductors, which is equivalent to that for silicon semiconductor.

Recently, we have established *pn*-control technique for organic semiconductors (Topic 1) and applied to the fabrication of the ohmic organic/metal contacts (Topic 2) and of the tandem cell formed in the codeposited film only by doping (Topic 3).

## 1. *pn*-Control and *pn*-Homojunction Formation in Single $C_{60}$ and $H_2Pc$ Films[1–3)]

Fullerene ($C_{60}$) and phthalocyanines are typical components in small-molecular-type organic photovoltaic cells. Based on experience with inorganic solar cells, to create a built-in potential, *pn*-control of highly purified organic semiconductors by doping is required.

In this study, complete *pn*-control and *pn*-homojunction formation were demonstrated for single $C_{60}$ films[1,2)] and for single metal-free phthalocyanine ($H_2Pc$) films.[3)] Cesium carbonate ($Cs_2CO_3$) and molybdenum oxide ($MoO_3$) were used as donor and acceptor dopants, respectively. Doping was performed by the coevaporation. Here, results on $H_2Pc$ films are summarized.

The Fermi level ($E_F$) of $H_2Pc$, located at the center of the bandgap (4.4 eV), is shifted to 3.8 eV, close to the conduction band (3.5 eV), by $Cs_2CO_3$ doping (5,000 ppm) and shifted to 4.9 eV, close to the valence band (5.1 eV), by $MoO_3$ doping (5,000 ppm) under oxygen free conditions (Figure 1). Formation of *n*- and *p*-type Schottky junctions and *pn*-homojunctions in single $H_2Pc$ films, confirmed by their photovoltaic properties, clearly demonstrates the formation of *n*- and *p*-type $H_2Pc$.

Moreover, the band bending can be also mapped in real scale based on the Kelvin probe measurements and the widths of depletion regions for *n*-type (Figure 2(a)), *p*-type (Figure 2(b)) Schottky junctions and *pn*-homojunction (Figure 2(c)) were determined to 23, 30, and 35 nm, respectively.

Conventionally, $H_2Pc$ and $C_{60}$ have been regarded as inherent *p*- and *n*-type semiconductors, respectively. However, *n*-$H_2Pc$ and *p*-$C_{60}$ can be formed by doping. So, it is reasonable that single organic semiconductors can, in general, be controlled to be *n*- or *p*-type, similar to inorganic semiconductors.

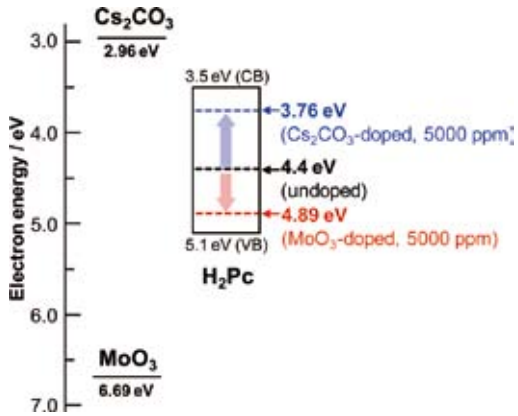


**Figure 1.** Energy diagram of a $H_2Pc$ film. The broken lines show the energy levels of $E_F$ for undoped (black), $MoO_3$-doped (red) and $Cs_2CO_3$-doped (blue) $H_2Pc$ films.

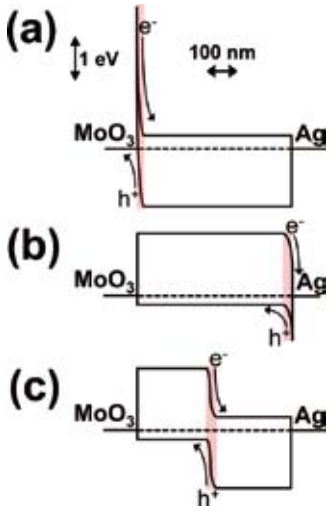


**Figure 2.** Energy structures for $Cs_2CO_3$-doped (a), $MoO_3$-doped (b), and $Cs_2CO_3$-/$MoO_3$-doped (c) cells in real scale based on the Kelvin probe measurements. Photocarrier generation occurs in the depletion regions (shaded).

## 2. Invertible Organic Photovoltaic Cells with Heavily Doped Organic/Metal Ohmic Contacts[4)]

In this study, we applied *pn*-control to make the two organic/metal contacts in a photovoltaic cell ohmic. Figure 3 shows the energetic structure for ITO/$n^+$-$C_{60}$ contact depicted based on the Kelvin probe measurements. 10,000 ppm $Cs_2CO_3$ was heavily doped in the vicinity of ITO electrode and made $C_{60}$ $n^+$-type. Though there is a distinct barrier to electrons with a height of 0.34 eV from the conduction band of $C_{60}$ to the ITO, since the band bends down steeply within 5 nm of the interface, photogenerated electrons can tunnel through this barrier. Thus, an ohmic contact is formed.

Heavily doped 10-nm-thick $p^+$- and $n^+$-type regions of $H_2Pc$ and $C_{60}$ were formed to facilitate the formation of ohmic contacts at the organic/metal interfaces of two-layered organic photovoltaic cells [ITO/$H_2Pc$/$C_{60}$/Ag]. Formation of the ohmic contacts allowed the cells to be invertible [ITO/$C_{60}$/$H_2Pc$/Ag] and independent of the type of electrode material used.

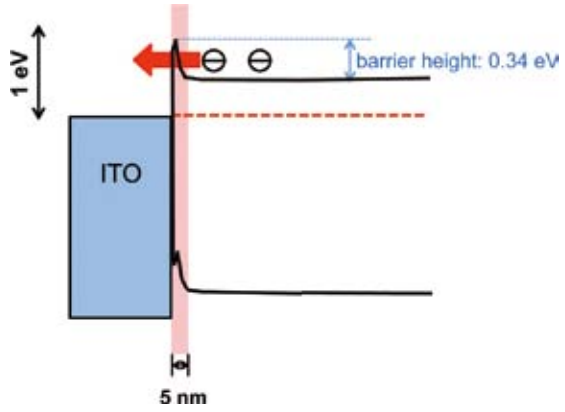


**Figure 3.** Energy structure for ITO/$n^+$-$C_{60}$ contact in real scale. A tunneling ohmic junction for photogenerated electrons is formed.

## 3. Tandem Organic Photovoltaic Cells Formed in Codeposited Films by Doping[5)]

*pn*-control technique should be extended to co-deposited films since organic solar cells should use co-deposited films to generate significant photocurrent densities based on the dissociation of excitons by the photoinduced electron transfer process.

In this study, tandem organic solar cells connecting two single homojunctions were formed in $C_{60}$:6T (α-sexithiophene) co-deposited films only by doping with $MoO_3$ and $Cs_2CO_3$ (Figure 4). Doping were performed by "three component co-evaporation."[6)] The single and tandem cells showed the open-circuit voltage of 0.85 and 1.69 V and conversion efficiency of 1.6 and 2.4%, respectively.

Figure 5 shows the energetic structure of tandem cell. Photocurrent is generated in the intrinsic (i) layers in front and back cells. Two single cells are connected by heavily doped $n^+p^+$-homojunction. Since the depletion region width of the $n^+p^+$-homojunction is extremely thin, *i.e.*, 20 nm, it can act as ohmic interlayer due to the carrier tunneling. Thus, the photovoltage of tandem cell (1.69 V) is doubled compared to that of single cell (0.85 V).

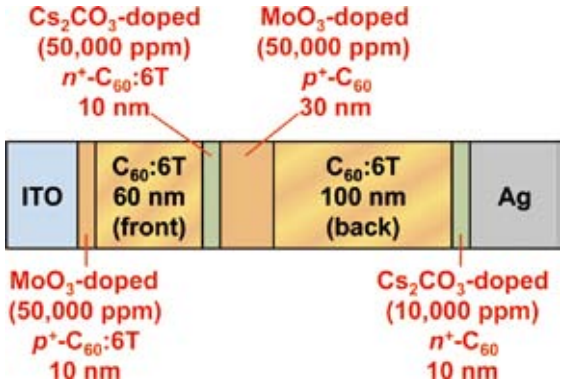


**Figure 4.** Structure of a tandem cell connecting two homojunction cells, which is made only by doping to $C_{60}$:6T codeposited film.

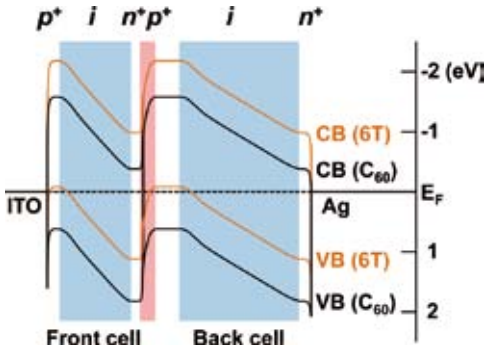


**Figure 5.** Energy structure of a tandem cell in real scale. $n^+p^+$-heavily doped homojunction acts as an ohmic interlayer connecting two single cells.

### References

1) M. Kubo, K. Iketaki, T. Kaji and M. Hiramoto, *Appl. Phys. Lett.* **98**, 073311 (2011).
2) M. Kubo, T. Kaji and M. Hiramoto, *AIP Adv.* **1**, 032177 (2011).
3) Y. Shinmura, M. Kubo, N. Ishiyama, T. Kaji and M. Hiramoto, *AIP Adv.* **2**, 032145 (2012).
4) M. Kubo, Y. Shinmura, N. Ishiyama, T. Kaji and M. Hiramoto, *Appl. Phys. Express* **5**, (2012), in press.
5) N. Ishiyama, M. Kubo, T. Kaji and M. Hiramoto, *Appl. Phys. Lett.*, submitted.
6) N. Ishiyama, M. Kubo, T. Kaji and M. Hiramoto, *Appl. Phys. Lett.* **99**, 133301 (2011).

### Award

KAJI, Toshihiko; Young Scientist Oral Presentation Award from Japan Society of Applied Physics (31st, 2011 Autumn Meeting).

# Development of Organic Semiconductors for Molecular Thin-Film Devices

**Research Center for Molecular Scale Nanoscience**
**Division of Molecular Nanoscience**

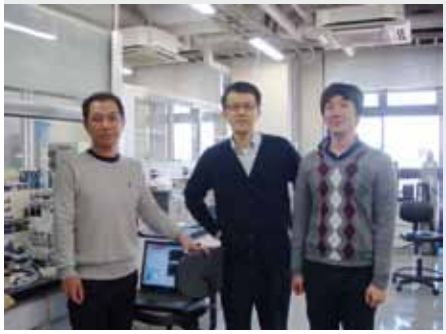

| | |
|---|---|
| SUZUKI, Toshiyasu | Associate Professor |
| SAKAMOTO, Youichi | Assistant Professor |
| KURODA, Yasuhiro | Post-Doctoral Fellow |
| WATANABE, Yoko | Secretary |


Organic light-emitting diodes (OLEDs) and organic field-effect transistors (OFETs) based on π-conjugated oligomers have been extensively studied as molecular thin-film devices. Organic semiconductors with low injection barriers and high mobilities are required for highly efficient OLEDs and OFETs. Radical cations or anions of an organic semiconductor have to be generated easily at the interface with an electrode (or a dielectric), and holes or electrons must move fast in the semiconducting layer. Compared with organic p-type semiconductors, organic n-type semiconductors for practical use are few and rather difficult to develop. Recently, we found that perfluorinated aromatic compounds are efficient n-type semiconductors for OLEDs and OFETs.

## 1. Selective Synthesis and Crystal Structure of [10]Cycloparaphenylene[1)]

[10]Cycloparaphenylene ([10]CPP) was selectively synthesized in four steps in 13% overall yield from commercially available 4,4'-diiodobiphenyl by using mono-I–Sn exchange, Sn–Pt transmetalation, I–Pd exchange, and subsequent oxidative coupling reactions. The structure of [10]CPP was determined by using single-crystal X-ray analysis. Suitable crystals were obtained by slow vapor diffusion of *n*-hexane into a solution of [10]CPP in $CH_2Cl_2$ at room temperature. In the solid state, [10]CPP is slightly distorted to an ellipsoidal structure with major and minor axes of 13.9 and 13.5 Å, respectively. The cavity of [10]CPP is occupied by a hexane molecule, which was highly disordered. Although the $D_{5h}$ structure with a dihedral angle between two paraphenylene units of 32°–33° was calculated to be the most stable conformer, the structure is closer to a $D_{2h}$ conformer with alternating triphenylene and biphenylene units. The dihedral angles between two paraphenylene units were approximately 20° and 45°, respectively. The average $C_{ipso}$–$C_{ipso}$, $C_{ipso}$–$C_{ortho}$, and $C_{ortho}$–$C_{ortho}$ bond lengths are 1.484(1), 1.399(2), and 1.385(9) Å, respectively. [10]CPP molecules pack in a herringbone manner, and there are no significant π–π interactions among [10]CPP molecules. A tilted tubular channel structure was observed along the *b* axis. The crystal packing is similar to [9]- and [12]CPPs but different from [6]CPP. The size of the CPP may be important for determining the packing arrangement.

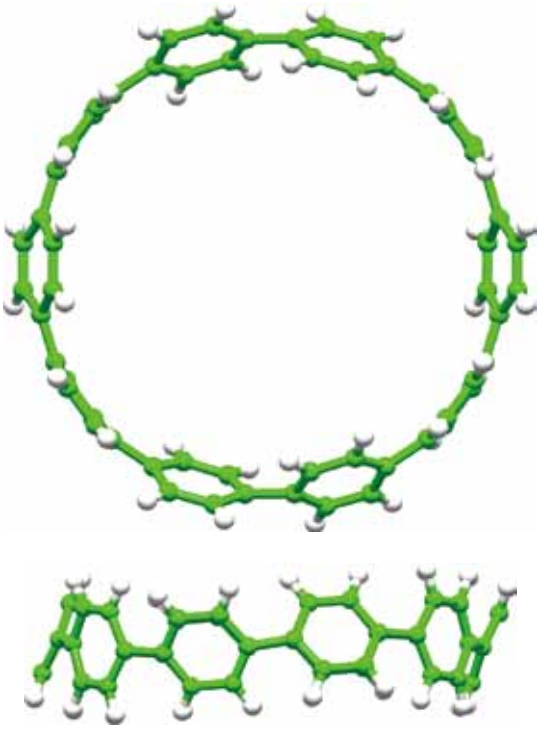

**Figure 1.** X-ray structure of [10]CPP.

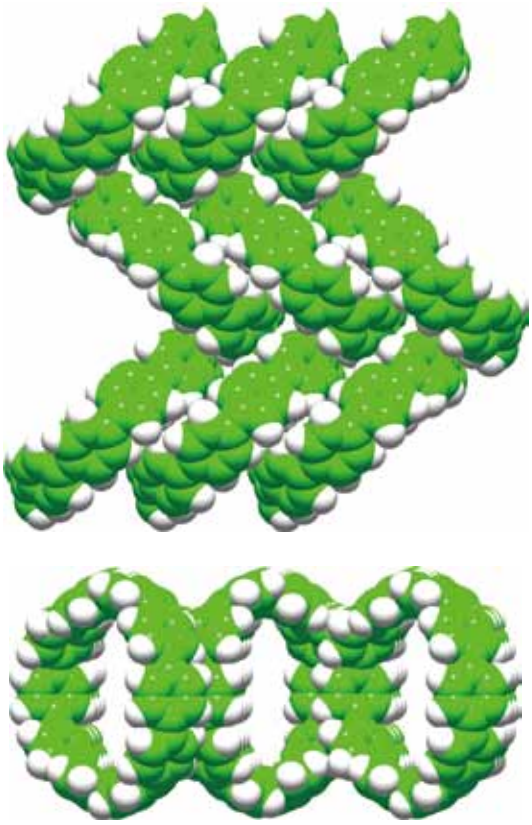

**Figure 2.** Packing structure of [10]CPP.

## Reference

1) E. Kayahara, Y. Sakamoto, T. Suzuki and S. Yamago, *Org. Lett.* **14**, 3284–3287 (2012).

# Building Photosynthesis by Artificial Molecules

**Research Center for Molecular Scale Nanoscience**
**Division of Molecular Nanoscience**

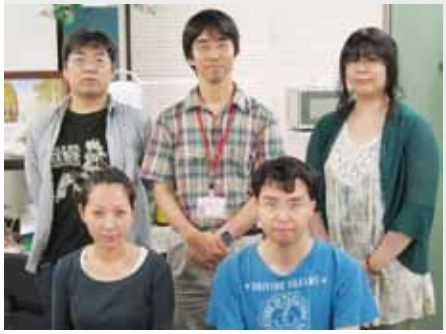

| | |
|---|---|
| NAGATA, Toshi | Associate Professor |
| SAKURAI, Rie | IMS Fellow |
| YUSA, Masaaki | Graduate Student |
| MIURA, Takahiro | Technical Fellow |
| WANATABE, Yoko | Secretary |


The purpose of this project is to build nanomolecular machinery for photosynthesis by use of artificial molecules. The world's most successful molecular machinery for photosynthesis is that of green plants—the two photosystems and related protein complexes. These are composed almost exclusively from organic molecules, plus a small amount of metal elements playing important roles. Inspired by these natural systems, we are trying to build up multimolecular systems that are capable of light-to-chemical energy conversion. At present, our interest is mainly focused on constructing necessary molecular parts and examining their redox and photochemical behavior.

## 1. Photoreduction of Quinones Sensitized by Soluble Phthalocyanines

Organic pigments are useful molecular parts for photosynthesis because of their ease of modification and high tunability. In particular, pigments for utilizing visible lights with long wavelength (>650 nm) are useful because they can complement the existing series of sensitizers for more efficient use of solar light. Phthalocyanines are good candidates as they have very strong absorption bands around 700 nm. However, studies on photochemistry of phthalocyanines are often hampered by the low solubility. To address this problem, we chose phthalocyanines (Pc) having 2,4-di-*t*-butylphenoxy substituents in the periphery. These phthalocyanines are so soluble in many organic solvents (even in hexanes!) that study of photoreactions in solutions can be easily carried out.

The target photoreaction is shown in Figure 1. The rate of reaction was dependent on the redox potentials of quinones, namely the reaction was faster for quinones with higher potential (*i.e.* more easily reduced). This indicates the reaction proceeds *via* photoinduced electron transfer from Pc to quinones. In particular, 2-*t*-butylanthraquinone and 2,6-dibutoxyanthraquinone did not react at all; these results suggest that the reaction proceeds *via* the triplet state of Pc ($^3$Pc) rather than the excited singlet state ($^1$Pc*), because $\Delta G$'s for the photoinduced electron transfer to these quinones were positive for $^3$Pc but negative for $^1$Pc*.


**Figure 1.** Photoreduction of quinones sensitized by soluble phthalocyanines with various central metals.

On the other hand, when different thiols were used as reductant, the rate of reaction was dependent on the acidity of thiols rather than the redox potential. Therefore, it is likely that the thiol works first as the proton donor to the anion radical of quinone, and then gives an electron to the cation radical of Pc (or to the neutral semiquinone radical).

When phthalocyanines with different central metal ions were employed, the rates of photoreaction were in the order Zn > Mg > Pd > 2H. Although the triplet quantum yield is higher for Pd than Zn, the photoreaction was very slow with Pd phthalocyanine. This is attributed to the high redox potential of PdPc, causing the photoinduced electron transfer unfavorable ($\Delta G$ = +0.17 eV for 2,5-di-*t*-butylbenzoquinone).

On the basis of these results, a plausible mechanism of this reaction is proposed as shown in Figure 2. Kinetic studies for important steps are currently underway. This study will lay an important cornerstone in utilization of low-energy photons for direct chemical conversions.

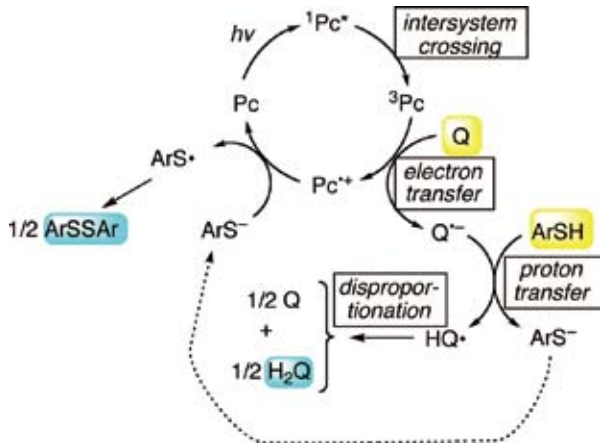


**Figure 2.** A plausible mechanism of photoreduction of quinones. Pc: phthalocyanine.

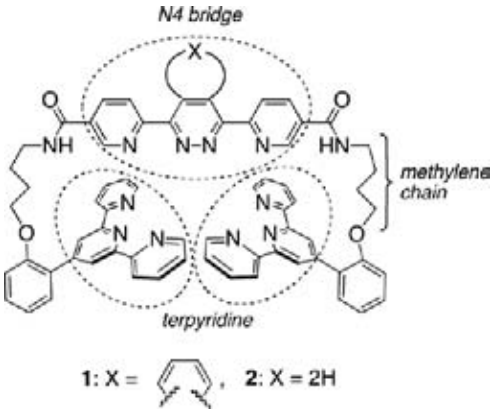


**Figure 3.** The ternary ligands consisting of two terpyridines and one "N4 bridge."

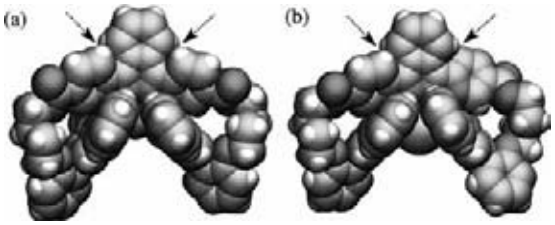


**Figure 4.** The space-filling drawing of the X-ray structures of (a) [(**1**)$Co_2$(μ-OH)]$^{3+}$ and (b) [(**1**)$Ni_2$(μ-Cl)]$^{3+}$.

## 2. Synthesis of Dinuclear Metal Complexes with Ternary Binucleating Ligands

As we already reported,[1)] combination of photochemistry of organic pigments and redox chemistry of transition metal complexes is a promising approach to develop new photoredox chemistry. In particular, use of first transition metals (3d metals) is worth studying, because they can provide crucial bridge between one-electron (photochemical) and two-electron (common organic chemical) processes. Synthesis of 3d metal complexes, however, is not always straightforward, because many 3d metal ions exchange ligands so easily that there are only limited choices of isolable compounds. In this respect, we can learn from biological systems where 3d metal complexes are utilized with a wide structural variation. This is made possible by the surrounding organic ligands (proteins).

Along this context, we prepared two new "ternary" ligands **1** and **2**, which consist of two terpyridines and one "N4 bridge" (1,4-bis(2-pyridyl)phthalazine for **1** and 3,6-bis(2-pyridyl) pyridazine for **2**). They formed stable dinuclear complexes [(**1**)$Co_2$(μ-OH)]$^{3+}$, [(**1**)$Ni_2$(μ-Cl)]$^{3+}$ and [(**2**)$Co_2$(μ-OH)]$^{3+}$. The X-ray structures of the first two complexes revealed subtle but characteristic differences (Figure 4). The steric repulsion between the hydrogen atoms at the *peri*-positions of the phthalazine ring and the 3-positions of the neighboring pyridine rings (indicated by arrows in Figure 4) caused twisting of the pyridine rings resulting in local axial chirality, and the stereochemistry of the axes were different between the Co and Ni complexes. In the Co complex, the two axes have the opposite axial stereochemistry, whereas in the Ni complex, the two axes have the same stereochemistry. Such difference was caused by the different ionic radii of the metal centers and by the different bridging anions ($OH^-$ and $Cl^-$).

The cyclic voltammogram of [(**1**)$Co_2$(μ-OH)]$^{3+}$ showed interesting behavior in the presence of acid (Figure 5). When triflic acid was added, the peaks of the $Co_2$ parts disappeared and new peaks corresponding to a mononuclear Co complex appeared instead. This change was attributed to the (reversible) release of one Co ion upon addition of acid.

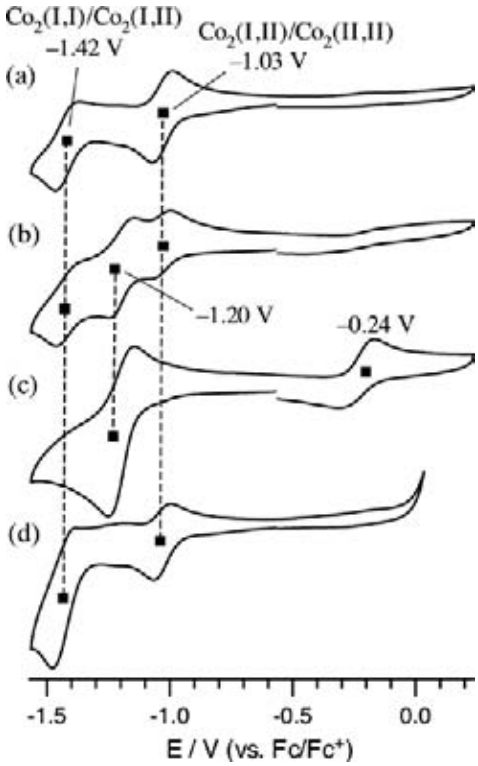


**Figure 5.** The changes of the CVs of [(**1**)$Co_2$(μ-OH)]$^{3+}$ with the addition of $CF_3SO_3H$ (a) 0 eq., (b) 1.0 eq., (c) 2.0 eq. and (d) after the addition of 5 eq. *i*PrNE$t_2$.

### Reference

1) H. Kon and T. Nagata, *Chem. –Eur. J.* **18**, 1781–1788 (2012).

# Chemistry of Bowl-Shaped Aromatic Compounds and Metal Nanocluster Catalysts

**Research Center for Molecular Scale Nanoscience**
**Division of Molecular Nanoscience**

| | |
|---|---|
| SAKURAI, Hidehiro | Associate Professor |
| HIGASHIBAYASHI, Shuhei | Assistant Professor |
| PANDA, Gautam | Visiting Scientist; JSPS Invited Fellow |
| MURUGADOSS, Arumugam | Visiting Scientist; JSPS Post-Doctoral Fellow |
| TAN, Qi-Tao | Visiting Scientist; JSPS Post-Doctoral Fellow |
| MORITA, Yuki | Post-Doctoral Fellow |
| SUGIISHI, Tsuyuka | Post-Doctoral Fellow |
| REZA, A. F. G. Masud | Visiting Scientist (JASSO Follow-up Research Fellow) |
| ANWER, Muslih | Visiting Scientist |
| SOPHIPHUN, Onsulang | Visiting Scientist |
| KAMONSATIKUL, Choavarit | Visiting Scientist |
| KOO, Jin Young | Visiting Scientist |
| ONOGI, Satoru | Graduate Student |
| DHITAL, Raghu Nath | Graduate Student |
| KARANJIT, Sangita | Graduate Student |
| SHRESTHA, Binod Babu | Graduate Student |
| KAEWMATI, Patcharin | Graduate Student |
| HAESUWANNAKIJ, Setsiri | Graduate Student |
| OKABE, Yuki | Graduate Student |
| SCHMIDT, Bernd | Graduate Student* |
| TOPOLINSKI, Berit | Graduate Student* |
| NAKANO, Sachiko | Technical Fellow |
| KIM, Yukimi | Technical Fellow |
| SASAKI, Tokiyo | Secretary |
| TANIWAKE, Mayuko | Secretary |
| HAZAMA, Kozue | Secretary |

Bowl-shaped π-conjugated compounds including partial structures of the fullerenes, which are called “buckybowls,” are of importance not only as model compounds of fullerenes but also as their own chemical and physical properties. For example, in solution they show the characteristic dynamic behavior such as bowl-to-bowl inversion. On the other hand, they sometimes favor stacking structure in a concave-convex fashion in the solid state, giving excellent electron conductivity. Furthermore, some buckybowls are conceivable to possess the bowl-chirality if the racemization process, as equal as bowl-to-bowl inversion, is slow enough to be isolated. Very few buckybowls has been achieved for preparation mainly due to their strained structure, and no report on the preparation of chiral bowls has appeared. In this project, we develop the rational route to the various buckybowls with perfect chirality control using the organic synthesis approach.

We also investigate to develop novel catalytic properties of metal nanoclusters. We focus on the following projects: Preparation of size-selective gold nanoclusters supported by hydrophilic polymers and its application to aerobic oxidation catalysts: Synthetic application using metal nanocluster catalyst: Development of designer metal nanocluster catalyst using the highly-functionalized protective polymers.

## 1. Enantioselective Synthesis of a Chiral Nitrogen-Doped Buckybowl[1)]

Bowl-shaped aromatic compounds, buckybowls, constitute a family of curved polycyclic aromatic carbons along with fullerenes and carbon nanotubes (CNTs). Doping of heteroatoms to the carbon frameworks of such aromatic compounds drastically modulates their physical and chemical properties. In contrast to nitrogen-doped azafullerenes or CNTs, synthesis of azabuckybowls, nitrogen-doped buckybowls, remains an unsolved challenging task. Accordingly, we have achieved the first enantioselective synthesis of a chiral azabuckybowl, triazasumanene. X-ray crystallographic analysis confirmed that the doping of nitrogen induces a more curved and deeper bowl structure than in all-carbon buckybowls. As a result of the deeper bowl structure, the activation energy for the bowl inversion (thermal flipping of the bowl structure) reaches an extraordinarily high value (42.2 kcal/mol). Since the bowl inversion corresponds to the racemization process for chiral buckybowls, this high bowl inversion energy leads to very stable chirality of triazasumanene.

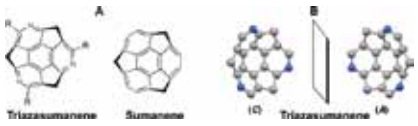

**Figure 1.** (A) Triazasumanene and sumanene; (B) Enantiomers of triazasumanene.

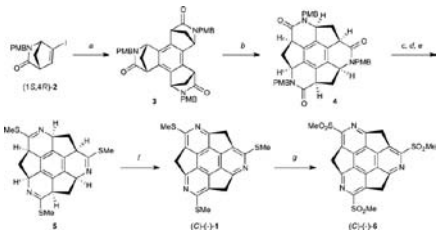

**Figure 2.** Conditions: (a) $Pd(OAc)_2$, $PPh_3$, $Bu_4NOAc$, $Na_2CO_3$, molecular sieve 4 Å, 1,4-dioxane, 100 °C, 2 h, 57%; (b) i) 12 M HCl, AcOH, 60 °C, 3 h; ii) $C_6F_5OP(=O)Ph_2$, DIPEA, DMF, 0 °C to 60 °C, 59% (two steps); (c) Lawesson’s reagent, dichloroethanene, microwave, 160 °C, 40 min, 92%; (d) Trifluoroacetic acid, microwave, 100 °C, 2 h, 88%; (e) MeI, $K_2CO_3$, DMF, 30 °C, 3 h, 79%; (f) $Ph_3CBF_4$, DTBMP, $CH_2Cl_2$, 25 °C, 3 d, 73%; (g) *m*-CPBA, $CH_2Cl_2$, 25 °C, 5 h, 90%.

## 2. Trimethylsumanene: Enantioselective Synthesis, Substituent Effect on Bowl Structure, Inversion Energy, and Electron Conductivity[2)]

$C_3$ symmetric chiral trimethylsumanene was enantioselectively synthesized through Pd-catalyzed *syn*-selective cyclotrimerization of an enantiomerically pure iodonorbornenone, ring-opening/closing olefin metathesis, and oxidative aromatization where the $sp^3$ stereogenic center was transmitted to the bowl chirality. Chiral HPLC analysis/resolution of the derivatives were also achieved. Based on theoretical calculations, the columnar crystal packing structure of sumanene and trimethylsumanene was interpreted as due to attractive electrostatic or CH–π interaction. According to the experimental and theoretical studies, the bowl depth and inversion energy were found to increase on methylation for sumanene in contrast to corannulene. Dissimilarities of the effect of methylation on the bowl structure and inversion energy of sumanene and corannulene were ascribed to differences in steric repulsion. A double-well potential model was fitted to the bowl structure-inversion energy correlation of substituted sumanenes, with a small deviation. The effects of various substituents on the sumanene structure and bowl inversion energy were analyzed by density functional theory calculations, and it was shown that the bowl rigidity is controlled by a combination of electronic and steric effects of the substituents. The electron conductivity of trimethylsumanene was investigated by time-resolved microwave conductivity method, compared with that of sumanene.

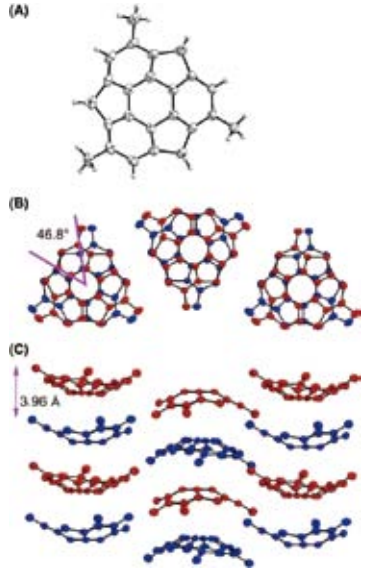


**Figure 3.** (A) ORTEP drawings of X-ray crystallographic analysis of (±)-**3**, (B) top view, (C) side view, shown at the 50% probability level.

## 3. Dual Roles of Polyhydroxy Matrices for Homocoupling of Arylboronic Acid Catalysed by Gold Nanoclusters Under Acidic Conditions[3)]

Polyhydroxy biopolymers including chitosan and starch play the dual roles of stabilization of gold clusters as well as activation of arylboronic acids through reversible binding. In acidic pH of 4.57 the electronic state of boron is changed to the corresponding to that at pH 9 inside the vicinity of Au:chit or Au:starch which favours the transmetallation process *i.e.* why homo-coupling product was observed even under acidic solutions.

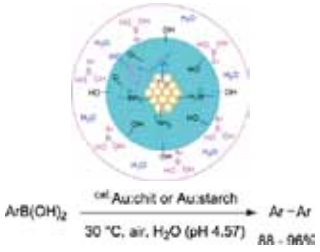


## 4. Anomalous Efficacy of Bimetallic Au/Pd Nanoclusters in C–Cl Bond Activation and Formal Metathesis-Type C–B Bond Activation at Room Temperature[4)]

Au/Pd alloy nanoclusters stabilized by poly (N-vinylpyrrolidone) catalyze two different reactions of phenylboronic acid with 4-chlorobenzoic acid at room temperature in a single reaction cycle, cross coupling and metathesis-type homocoupling that is normally inaccessible through conventional catalysis.


### References

1) Q.-T. Tan, S. Higashibayashi, S. Karanjit and H. Sakurai, *Nat. Commun.* 3:891 doi: 10.1038/ncomms1896 (2012).
2) S. Higashibayashi, R. Tsuruoka, Y. Soujanya, U. Purushotham, G. N. Sastry, S. Seki, T. Ishikawa, S. Toyota and H. Sakurai, *Bull. Chem. Soc. Jpn.* **85**, 450–467 (2012).
3) R. N. Dhital, A. Murugadoss and H. Sakurai, *Chem. –Asian J.* **7**, 55–59 (2012).
4) R. N. Dhital and H. Sakurai, *Chem. Lett.* **41**, 630–632 (2012).


### Awards

DHITAL, Raghu Nath; Young Scientist Award, International Conference on Advanced Materials and Nanotechnology (2011).
DHITAL, Raghu Nath; Young Oral Presentation Award, International Symposium on Catalysis and Fine Chemicals 2011 (2011).
TAN, Qi Tao; Outstanding Poster Presentation, International Symposium on Catalysis and Fine Chemicals 2011 (2011).

* carrying out graduate research on Cooperative Education Program of IMS with Freie Universität Berlin

# Spectroscopic Studies on Electronic Ferroelectricity in Organic Conductors

**Department of Materials Molecular Science**
**Division of Electronic Properties**

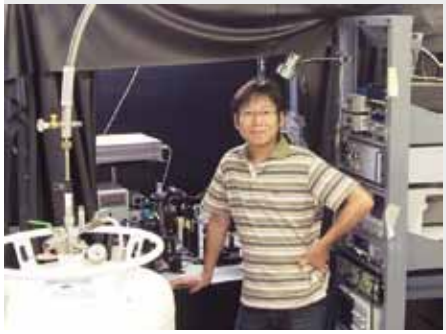

YAMAMOTO, Kaoru Assistant Professor

Organic conductors exhibit unusual physical properties due to the critical nature of valence electrons fluctuating under localizing and delocalizing regime. Recently, we discovered that an organic superconductor, α-(BEDT-TTF)$_2$I$_3$ [BEDT-TTF: bis(ethylenedithio)tetrathiafulvalene], induces optical second-harmonic generation (SHG) along with charge-ordering driven by the repulsive electron-electron interactions.[1] The SHG activity proves that the organic complex induces macroscopic electric polarization by the electronic transition. To understand the fundamental and functional properties of such "electronic ferroelectrics," we are engaged in the material research and development of experimental technique dedicated for low-temperature SHG microscopy of tiny organic crystals.

## 1. SHG Microscopy of Ferroelectric Organic Conductor Using Hydrostatic Pressure Apparatus with Argon as a Heat Transfer Medium[2]

To perform nonlinear microscopy at low-temperatures, one has to dissipate the excessive heat from the photo-irradiated spot of the sample without affecting the physical properties. In the present study, we designed a sapphire-anvil cell, which is usually adopted for high-pressure measurements, as a cooling apparatus used along with liquid-argon as heat-transfer medium. The cryogenic performance of the argon-loaded sapphire cell was examined by the observation of SHG of an organic conductor α'-(BEDT-TTF)$_2$IBr$_2$ at low temperatures.

This α-type compound is unusually susceptible to mechanical stress. In a previous study, we have embedded the single crystals of the compound into a polymer resin and sandwiched them by sapphire plates, and observed the SHG at low temperatures. Because of the difference in thermal shrinkage between the samples and the sapphire plates, the crystals were fragmented with decreasing temperature. The observed image of SHG showed distinct inhomogeneity; the nonlinear optical signal was generated only from limited areas of the crystals, suggesting that the single crystals were divided into ferroelectric and antiferroelectric regions, presumably due to the mechanical stress.

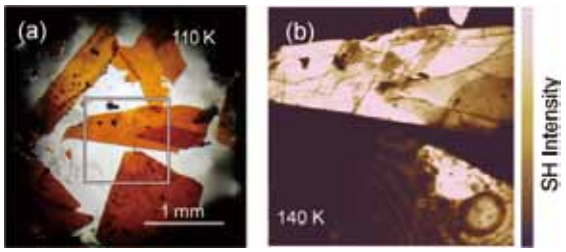


**Figure 1.** (a) Thin crystals of α'-(BEDT-TTF)$_2$IBr$_2$ in a sapphire-anvil cell loaded with liquid argon. (b) SHG image in the square region of (a) ($T$ = 140 K).

Figure 1(a) shows the transmission image of the filmy thin crystals of the complex mounted in the sapphire cell loaded with liquid argon. The crystals cooled via the heat transfer medium were not completely intact, but the pieces of the cleaved crystals were much larger than the above mentioned fragmented crystals. As shown by the SHG image [Figure 1(b)], the cleaved crystals generated SHG from their whole region. This fact proves that the compound is a bulk ferroelectric matter, and at the same time, indicates that the heat at the irradiated spot was efficiently dissipated via the heat transfer medium without applying severe mechanical stress to the sample.

The successful SHG observation demonstrates that the cooling technique is helpful for low-temperature measurements of nonlinear optical microscopy requiring high-density photo-excitations.

### References

1) K. Yamamoto, *et al.*, *J. Phys. Soc. Jpn.* **77**, 074709 (2008).
2) K. Yamamoto, *et al.*, *Phys. Status Solidi C* **9**, 1189 (2012).

# Multifunction Integrated Macromolecules for Molecular-Scale Electronics

**Research Center for Molecular Scale Nanoscience**
**Division of Molecular Nanoscience**

TANAKA, Shoji Assistant Professor

Recently a single electron tunnel (SET) device has attracted much attention due to the growing demand for ultra-low-power device. A SET device manipulates an electron by means of one-by-one electron transfer, resulting in ultimately low power consumption. However, for room temperature operation, the size of SET device must be as small as a few nm to overcome the thermal fluctuation problems. The process size of a few nm is out of the range of conventional micro-technology. In this project, to establish an innovative fabrication process for SET device systems, we have been developing step-wise synthetic protocols for monomolecular single-electron tunnel devices (**MOSET**) and their integrated circuits.

## 1. Universal Temperature Crossover Behavior of Electrical Conductance in a Single Oligothiophene Molecular Wire[1)]

We have observed and analyzed a universal temperature crossover behavior of electrical conductance in a single oligothiophene molecular wire. The crossover between the Arrhenius type temperature dependence at high temperature and the temperature-invariant behavior at low temperature is found at a critical molecular wire length of 5.6 nm, where we found a change from the exponential length dependence to the length-invariant behavior. We have derived a scaling function analysis for the origin of the crossover behavior. After assuring that the analysis fits the explanation of the Keldysh Green's function calculation for the temperature dependence, we have applied it to our experimental results and found successfully that our scaling function gives a universal description of the temperature dependence for all over the temperature range.

## 2. Fabrication of 3- and 4-Terminal Single-Electron Device Structures

To integrate Coulomb islands and tunnel/capacitive junctions in a single molecular skeleton, we have developed a series of molecular building blocks (**1**–**8**). These building blocks make possible to fabricate various type of 3- and 4-terminal monomolecular single-electron tunnel device structures (**11**, **13**, **17**).

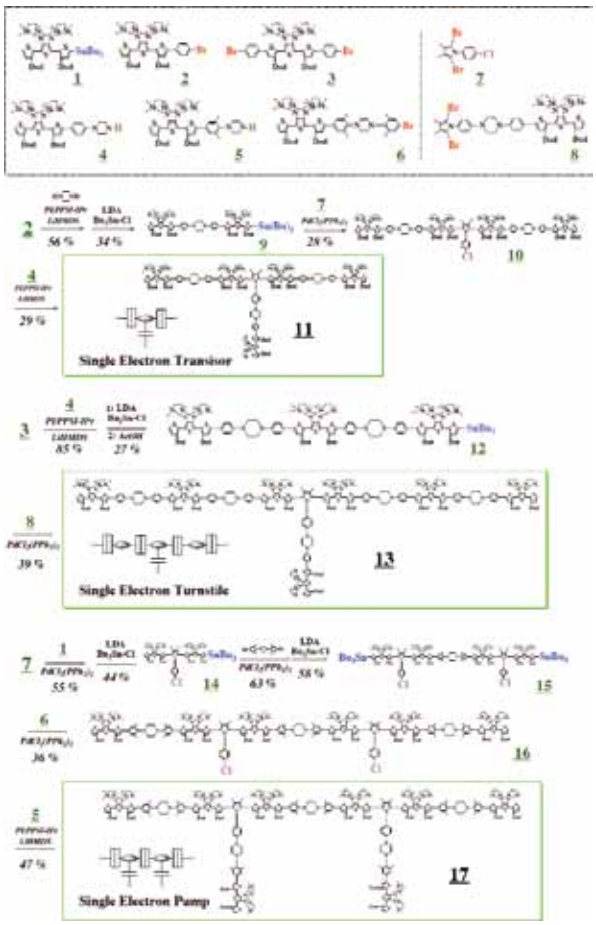


Reference

1) SK. Lee, R. Yamada, S. Tanaka, GS. Chang, Y. Asai and H. Tada, *ACS Nano* **6**, 5078–5082 (2012).

# Development of Novel Heterocyclic Compounds and Their Molecular Assemblies for Advanced Materials

**Safety Office**

TOMURA, Masaaki Assistant Professor

Heterocycles containing sulfur and/or nitrogen atoms are useful as components of functional organic materials since heteroatoms in their rings are helpful to stabilize ions or ion-radical species. In addition, intermolecular interactions caused by heteroatom contacts can be expected to form unique molecular assemblies. In this project, novel functional organic materials based on various heterocycles were synthesized and their physical and structural properties were investigated.

## 1. Molecular and Crystal Structure of Bis(tetra-*n*-butylammonium) Bis(5,6-dicyanopyrazine-2,3-dithiolato-$\kappa^2$*S*,*S*') palladium(II)[1)]

Metal dithiolene complexes have been widely investigated as molecular conductors and superconductors. Several superconductors and single-component molecular metals involving dithiolene complexes have been discovered to date. We have synthesized the title palladium dithiolene complex derived from 2,3-dicyano-5,6-dimercaptopyrazine ligand. The ligand is expected to extend the π-conjugation of the complex resulting in decreased Coulombic repulsion. Intermolecular interactions caused by S···S and S···N heteroatom contacts may increase the dimensionality in the solid state. In the complex the dianion molecule is located on an inversion center. The dianion is a flat molecule with an r.m.s. deviation of 0.034(8) Å of fitted atoms from the least-squares plane. The central Pd atom has a square-planar coordination geometry and the Pd–S distances and the S–Pd–S angle are 2.276(3), 2.294(3) Å and 89.39(10)°, respectively. These values are comparable to those found in bis(tetra-*n*-butylammonium) bis(4,5-dicyanobenzene-1,2-di- thiolato-*S*,*S*')palladium(II) complex. The dianion molecules form a layered structure with an interlayer distance of 6.5 Å. The tetra-*n*-butylammonium cations are inserted between the layers.

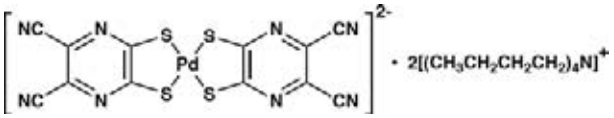


## 2. Photoinduced Electron-Transfer Reaction of α-Bromomethyl-Substituted Benzocyclic β-Keto Esters with Amines: Selective Reaction Pathways Depending on the Nature of the Amine Radical Cations

Photoinduced electron-transfer reaction of α-bromomethyl-substituted benzocyclic β-keto esters with tertiary amines was investigated. Debrominated β-keto esters and ring-expanded γ-keto esters were obtained as major products. On the basis of mechanistic experiments it was concluded that these products are formed via a reaction sequence of selective carbon–bromine bond cleavage and subsequent competitive hydrogen abstraction and Dowd–Beckwith ring-expansion of the resulting primary alkyl radicals. The characteristic product distribution observed for the type of amine used is rationalized on the basis of selective reaction pathways of generated radical intermediates that depend on the nature of the amine radical cations.

### Reference

1) M. Tomura and Y. Yamashita, *Acta Crystallogr., Sect. E: Struct. Rep. Online* **68**, m57–m57 (2012).

# Visiting Professors

Visiting Professor
**ABE, Manabu** *(from Hiroshima University)*

Stretch Effects Induced Molecular Strain in Generating Long-Lived Biradicals

Stretch effects induced by two types of molecular strain were examined by quantum chemical calculations, to design persistent multi-radicals such as localized diradicals and oxyallyls. The cooperative molecular strain (Type-1) induced by the spiro[5.5]undecane and bicyclo[2.1.0]cyclopentane structures was found to significantly destabilize in energy the ring-closed compounds of the diradicals, leading to small energy differences between the diradicals and the σ-bonded compounds. Another stretch effect (Type-2) induced by macrocyclic systems was also found to energetically destabilize the corresponding ring-closed structures of the 1,3-diradicals. The computational studies predict that the two types of stretch effects are quite effective in lowering the energy barriers of the bond-breaking reaction of the ring-closed compounds and in generating long-lived localized diradicals and oxyallyl derivatives.

Visiting Professor
**KATO, Tatsuhisa** *(from Kyoto University)*

Studies of Molecular Magnetization of Super-Molecules

The encapsulation of $C_{60}$ with γ-cyclodextrin (γ-CD) has been attained by a mechanochemical high-speed vibration (HSV) technique. N@$C_{60}$, which can be a good magnetic probe giving the information of position as well as of chemical environment, should be soluble in water for the purpose of biological application. Then the HSV technique was applied to the powder of γ-CD and $C_{60}$ containing N@$C_{60}$ at 5%. The obtained molecular complex exhibited the peculiar electron spin resonance (ESR) spectrum of N@$C_{60}$ in water.

We designed the flexible intermolecular communications in a simple molecular architecture by using mechanically interlocked supramolecular motives such as catenanes and rotaxanes, in which two or more molecular components are inseparable but their interactions are flexibly convertible. In a dinuclear $Cu^{2+}$ complex of the four-fold rotaxane, the $Cu^{2+}$-porphyrin and the $Cu^{2+}$-phthalocyanine were stacked efficiently on one another to afford spin–spin communication. Spin states of the dinuclear complex were switchable between its protonated form (doublet) and deprotonated form (singlet) reversibly.

Visiting Professor
**ASAKURA, Tetsuo** *(from Tokyo University of Agriculture and Technology)*

Determination of Molecular Structure with Ultra Fast MAS under High-Field NMR

In single crystal X-ray diffraction analyses of peptides and proteins, it is well-known that the co-ordinates of carbon, nitrogen and oxygen atoms can be obtained in high accuracy, but enough accuracy cannot be obtained for those of hydrogen. Therefore we are trying to determine the accurate $^1$H positions by the combination of NMR observation by ultra fast magic angle spinning under high field magnetic field and accurate $^1$H NMR chemical shift calculation. We are applying this novel analytical technique to determine the structures of silk fibroins before and after spinning together with their model peptides. Since such a $^1$H information is sensitive to both the intra- and inter -molecular structures, it is especially useful in molecular design of biomaterials with silks.